LITHOS 428-429 (2022) 106813

Contents lists available at ScienceDirect

LITHOS

journal homepage: www.elsevier.com/locate/lithos

Carbon mobility and exchange in a plate-interface subduction mélange: A case study of meta-ophiolitic rocks in Champorcher Valley, Italian Alps

M. Scambelluri [a,*], E. Cannaò [b], S. Guerini [b], G.E. Bebout [c], G.S. Epstein [c], F. Rotondo [d], N. Campomenosi [e], P. Tartarotti [b]

[a] Dipartimento di Scienze della Terra, Ambiente e Vita, Università di Genova, C.so Europa 26, 16132 Genova, Italy
[b] Dipartimento di Scienze della Terra "A. Desio", Università di Milano, Via Botticelli 23, 21133 Milano, Italy
[c] Department of Earth and Environmental Sciences, Lehigh University, Bethlehem, PA 18015, USA
[d] National Oceanography Centre Southampton, University of Southampton, United Kingdom
[e] Mineralogisch-Petrographisches Institut, Universität Hamburg, Germany

ARTICLE INFO

Keywords:
Subduction
Carbon mobility
Fluids
Carbonatic rocks
Serpentinite

ABSTRACT

Ultramafic and carbonate-rich rocks juxtaposed in an oceanic sedimentary mélange that experienced Alpine subduction (Champorcher, Aosta Valley, Italy) show evidence of metasomatic alteration at their contacts. The reactions that occurred at these contacts afford an assessment of the sources and compositions of fluids associated with the alteration, the degree and scale at which these reactions mobilized carbon. At these contacts, carbonate-rich rocks display calcite replacement by diopside and tremolite along foliations and pressure-dissolution planes as the result of decarbonation and/or carbonate dissolution. The associated ultramafic bodies record serpentine replacement by carbonates and formation of metamorphic veins hosting carbonate and carbonate + diopside + chlorite. These two sets of observations point to coeval, coupled decarbonation and carbonation reactions resulting in C mobility along the subduction interface (at about 60 km depth) but conceivably without considerable net loss and large-scale transport.

The $\delta^{18}O_{V\text{-}SMOW}$ values of all the samples analyzed in this study are lower than expected for oceanic protoliths (for marine limestone, carbonate with values of +28 to +30‰; for seafloor ophicarbonate somewhat lower), suggesting pervasive interaction of these rocks with externally derived fluids, as has been observed throughout the region (for calcschists such as the Schistes Lustrés, lowering values to +20 ± 2‰). The calcschist unit at Champorcher has $\delta^{18}O$ (+21.9 to +23.6‰) falling into this regionally developed range; however, the other rocks at this locality (carbonate mélange/broken formation, metasomatic rinds, and veins) tend to have lower values (to as low as +13.5‰). These lower values appear to require interaction with a fluid with $\delta^{18}O$ lower than that affecting the calcschist on a regional scale and more consistent with derivation from a mafic/ultramafic (ophiolitic) source. Some metamorphic veins showing carbonate $\delta^{18}O$ values 1 to 2‰ lower than their hosts and the occurrence of metamorphic veins and metasomatic horizons with anomalously high $^{87}Sr/^{86}Sr$ point to circulation of isotopically distinct external fluids enriched in radiogenic Sr within the Champorcher suite, perhaps involving a source in devolatilizing terrigenous rocks.

Juxtaposition of rocks at scales observed in these mélange units could enhance the mobilization of C *via* decarbonation reactions if this deformation is accompanied by the infiltration by H_2O-rich fluids capable of driving the reaction process. Information regarding the metasomatism within this hybrid carbonate-ultramafic unit bears on the question of C mobilization along subduction interfaces and whether the magnitude of any loss or gain at the scales investigated could significantly influence whole-margin C cycling.

1. Introduction

In the last decades, much work has been focused on the deep Earth carbonate-silicate geochemical cycle and its effect on the release of atmospheric carbon (C) (Bebout, 2014; Dasgupta and Hirschmann, 2010; Jarrard, 2003; Kerrick and Connolly, 1998). The cycling of C into the

* Corresponding author.
E-mail address: marco.scambelluri@unige.it (M. Scambelluri).

https://doi.org/10.1016/j.lithos.2022.106813
Received 19 February 2022; Received in revised form 20 July 2022; Accepted 21 July 2022
Available online 26 July 2022

deep Earth occurs at subduction zones, where devolatilization of oceanic and continental slabs release volatile and fluid-mobile elements to the supra-subduction mantle (*e.g.*, Cannaò and Malaspina, 2018). Fluid-fluxed melting in the mantle wedge transfers volatile components such as CO_2 into arcs and, through volcanic degassing, into the atmosphere (Collins et al., 2015; Dasgupta, 2013). This so-called slow C cycle has kept Earth habitable over geological timescales (Dasgupta, 2013).

In subduction zones, the plate interface is the key domain where deformation, fluid flow, fluid/rock exchange and element transfer become highly focussed (Agard et al., 2018; Bebout and Penniston-Dorland, 2016). This domain is currently under multidisciplinary investigation and several models have been conceived to explain its architecture and evolution through time and space (Gerya et al., 2002; Ruh et al., 2015). The plate interface lithological assemblages mainly consist of hydrated (serpentinized) wedge mantle and/or top-slab sediments tectonically mixed with slices of slab crust and mantle materials of varying sizes (Agard et al., 2018; Bebout and Penniston-Dorland, 2016). The plate interface can also consist of sedimentary mélanges formed in oceanic abyssal planes and/or in accretionary complexes near subduction trenches, which transform into tectonized top-slab metasedimentary sequences during subduction processing and infiltration of slab fluids (Breeding et al., 2004; Bebout and Penniston-Dorland, 2016; Festa et al., 2019).

The subduction cycle and the residency of C in subducting plates, at the plate interface, and in the supra-subduction mantle is a debated and timely issue. Experiments and thermodynamic modeling of decarbonation reactions indicate stability of carbonate minerals to very high pressures (*P*) and temperatures (*T*), suggesting minimal C loss from rocks to fluids, particularly to depths of ~80 km, in the deep forearc/subarc (Molina and Poli, 2000; Thomsen and Schmidt, 2008; Poli et al., 2009; Cook-Kollars et al., 2014; Collins et al., 2015; Menzel et al., 2020; Epstein et al., 2021b). Carbonate reduction to graphite by fluid–rock interaction can also affect C retention in subducting rocks (Galvez et al., 2013; Giuntoli et al., 2020; Vitale Brovarone et al., 2017). On the other hand, significant C mobility in the deep forearc and beneath arcs (> 80 km), can be deduced by high CO_2 output from arc volcanoes (Epstein et al., 2021b; Hilton et al., 2002), by experimental evidence (Caciagli and Manning, 2003), and by the fluid inclusion and mineral record preserved in (ultra) high-*P* rocks and subarc xenoliths (Frezzotti et al., 2011; Malaspina et al., 2009; McInness and Cameron, 1994; Sapienza et al., 2009; Scambelluri et al., 2016; Stöckhert et al., 2001; Van Roermund et al., 2002). In subduction zones, decarbonation reactions are enhanced by the infiltration of carbonate-bearing rocks by H_2O-rich fluids (Collins et al., 2015; Cook-Collars et al., 2014; Dolejs and Manning, 2010; Gorman et al., 2006); carbonate dissolution can also be facilitated by this infiltration (Caciagli and Manning, 2003; Dolejs and Manning, 2010; Sanchez-Valle et al., 2003; Frezzotti et al., 2011; Ague and Nicolescu, 2014; Menzel et al., 2020; Muñoz-Montecinos et al., 2021).

Multiple lines of evidence thus point to C mobility in subduction zones, although the depth range over which the bulk of this mobility occurs and the magnitude and the exact mechanisms of extraction remain uncertain (Ague and Nicolescu, 2014; Collins et al., 2015; Cook-Collars et al., 2014; Poli et al., 2009). Some recent studies of high-*P* rocks show that interaction of carbonate-bearing rocks with H_2O-rich fluids leads to carbonate breakdown and formation of aqueous-carbonic fluids (Ague and Nicolescu, 2014; Stewart and Ague, 2020). The latter are highly reactive with mafic and ultramafic rocks encountered along the flow pathway and induce rock carbonation and formation of subduction ophicarbonates (Cannaò et al., 2020; Piccoli et al., 2016; Scambelluri et al., 2016). Here, it is important to note that, although several mechanisms of C mobilization have been demonstrated in field studies of metamorphic rocks, the scale at which this mobility occurs tends to be meters to tens of meters and it has proven difficult to extrapolate these observed processes to scales impacting whole-margin C cycling (see the discussion by Epstein et al., 2020). In this respect, still poorly explored is the potential of pressure dissolution processes in subduction-zone rocks in terms of mineral dissolution, mass loss and impact on fluid compositions (Muñoz-Montecinos et al., 2021; Stöckhert, 2002; Van Schrojenstein Lantman et al., 2021).

Subduction-zone mélanges hosting hydrated silicate-rich rocks embedded in a carbonate-rich matrix are thus natural laboratories to investigate the interplay of aqueous fluids with carbonates, the release of C to fluids and the reactivity of the carbonic fluids with the surrounding rock-types. Here, we show the petrologic and geochemical subduction record of a top-slab, oceanic sedimentary mélange exposed in the Champorcher valley (Zermatt-Saas Ophiolite, Western Alps). The mélange corresponds to a Composite Chaotic Unit (CCU) consisting of ultramafic clasts and blocks embedded in a carbonate matrix. This CCU overlies a serpentinite and ophicarbonate basement and is overlain by layered metasedimentary unit dominated by calcschist (CSU). According to field investigations, the chaotic unit formed in response to intra-oceanic extensional faulting exposing mantle rocks on the seafloor of the Tethyan ocean and to sedimentation of carbonaceous turbidite (Tartarotti et al., 2017), fluid infiltration, and metamorphism (Tartarotti et al., 2019). Formation of new silicate minerals at the expense of the carbonate rocks and serpentinite carbonation point to C transfer in fluids and fluid/rock interaction during the subduction evolution of this mélange (Rotondo et al., 2021; Tartarotti et al., 2019). Our aim is documenting C exchange and mobility during subduction of this top-slab sedimentary mélange using detailed petrology, C—O stable isotope geochemistry, and Sr isotopes to unravel the open *vs.* closed system evolution of the system (*e.g.,* Cannaò et al., 2020).

2. Geological and petrological background

The rocks investigated here belong to the high-*P* Zermatt-Saas metaophiolite unit of the Western Alps (*i.e.,* the "Zermatt Saas Zone"). The Alpine orogenic belt originated from Late Cretaceous to Oligocene convergence between the paleo-European and Adriatic plates. During this process, subduction of the extended continental margins and of the interposed Jurassic oceanic Tethys was followed by exhumation of the high-*P* rocks and by collision of the two continental plates (Polino et al., 1990; Dal Piaz et al., 2001; Beltrando et al., 2010). The 160 Ma old Tethys was an analogue of the present-day slow and ultraslow spreading oceans like the Atlantic, which are floored by a lithosphere made of dominant mantle peridotite intruded by discrete km-sized gabbroic bodies topped by basaltic lavas and pelagic sediments (Lagabrielle and Cannat, 1990). Serpentinization and carbonation intensely affected the mantle peridotites during exposure near the seafloor, and/or along detachment faults activated by the oceanic extensional tectonics. In several Alpine and Apennine occurrences, serpentinized mantle rocks can be directly overlain by basaltic pillow lavas, by sedimentary and tectonic breccias and by carbonaceous sediments (Marroni and Pandolfi, 2007; Tartarotti et al., 2017 and references therein). During Alpine subduction in the time span between *ca.* 80 and 38 Ma (Dal Piaz et al., 2001; Rubatto et al., 1999; Manzotti et al., 2018; Rebay et al., 2018; Starr et al., 2020), the oceanic basement and its volcano-sedimentary cover transformed into high- to ultrahigh-*P* metaophiolites and experienced intensive fluid/rock exchange (Reinecke, 1991; Bucher et al., 2005; Groppo et al., 2009; Frezzotti et al., 2011; Haws et al., 2020). The Zermatt-Saas Zone mostly consists of serpentinites, metagabbros, metarodingites, and metabasalts including Fe—Cu ore bodies, all covered by micaschists, calcschists, marble, and metaquartzites. It has been intensively studied in the last fifteen years: the mafic and ultramafic rocks forming this high-*P* metaophiolite display similar burial and exhumation *P*–*T* paths, suggesting subduction depths around 70–80 km (~ 23–25 kbar, 530–550 °C; Angiboust et al., 2009; Li et al., 2004; Rebay et al., 2012). Small lenses associated with the Zermatt-Saas complex could have reached greater depths (the Lago di Cignana unit ~26–28 kbar), as suggested by coesite and diamond inclusions in garnet (Frezzotti et al., 2011; Groppo et al., 2009; Reinecke, 1991) and, presumably, by

Ti-Clinohumite and Ti-Chondrodite in serpentinites (Valtournanche ~28–35 Kbar and 600–670 °C).

We focused our study in the high Champorcher Valley (southern Aosta Valley, Italy; Fig. 1A). In this area and in the surroundings, tectonic units of both continental and oceanic origin showing a high-*P* and low-*T* alpine metamorphic imprint are tectonically juxtaposed (Dal Piaz et al., 2001; Beltrando et al., 2007, 2008; Ellero and Loprieno, 2017; Tartarotti et al., 2017; Rotondo et al., 2021). In the Southern Aosta Valley numerous tectonic units of metaophiolites share structural and metamorphic features and are commonly attributed to the Zermatt-Saas Zone (Beltrando et al., 2008; Ellero and Loprieno, 2017; Tartarotti et al., 2019). Metaophiolites from this area and, more specifically, in the high Champorcher Valley are dominated by oceanic mantle rocks composed of antigorite-bearing serpentinites with metamorphic olivine and Ti-clinohumite, and rare pre-Alpine (*i.e.,* oceanic) mineralogical relics, Mg-Cr-rich metagabbros, metarodingites, and smaller amounts of mafic rock with metatrondhjemite composition (Fontana et al., 2015). As in the Zermatt-Saas Zone *s.s.*, these metaophiolites show a dominant early Alpine subduction-related blueschist-eclogite facies imprint of Eocene age, to varying degrees retrogressed under greenschist-facies conditions (Tartarotti et al., 2019 and references therein). In southern Aosta Valley, the Zermatt-Saas unit records early Alpine blueschist- to eclogite-facies metamorphism; the peak P-T conditions achieved appear to be the same as in the entire Zermatt-Saas Zone but the rocks are more affected by late-stage metamorphism and hydration (Dragovic et al., 2020).

Two main types of oceanic metasedimentary successions are recognizable in the southern Aosta Valley (Tartarotti et al., 2017). The first comprises metaradiolarite, marble, calcschists *s.s.*, and flysch-like calcschists (Tartarotti et al., 2017) that commonly cover metabasalts with sulphide-ore deposits or metagabbros (Martin et al., 2008; Rebay et al., 2012; Tumiati et al., 2010). The second succession consists of a serpentinized mantle peridotite basement overlain by ophicarbonate breccias or mixed mafic-ultramafic clasts in a carbonatic matrix that are topped by flysch-like calcschists with ophiolitic interbeds (*e.g.,* Tartarotti et al., 2017). This second type of metasedimentary sequence is well exposed in the high Champorcher Valley (Figs. 1B, C), where it consists of the Composite Chaotic Unit (CCU), characterized by a block-in-matrix texture showing ultramafic clasts and blocks embedded within a foliated carbonate matrix. Several domains showing varying textures and composition have been recognized in the CCU based on clast or block size, shape, and composition and on the matrix/clast ratio (Tartarotti et al., 2017); the contacts between the various domains are gradational, preventing a clear distinction among different types. These textures have been attributed to mass transport deposits triggered by fault scarps and to turbiditic sedimentation (Tartarotti et al., 2017) and are comparable to those typical of broken-formations and of sedimentary mélanges. Pervasive ductile deformation related to the Alpine subduction intensely disrupted the original fabric to develop shear structures and metasomatic horizons as the result of intense fluid-rock interaction during ongoing subduction in a fluid-assisted environment.

3. Methodology

3.1. Analytical methods

Major and minor element concentrations (including Ni and Sr) were determined on selected samples using a JEOL 8200 Super Probe equipped with 5 WDS spectrometers and an EDS and housed at the Department of Earth Science "Ardito Desio" of the University of Milan. The operating conditions were as follows: 15 kV of acceleration voltage on the tungsten filament and 5 nA of current electron beam with a point analysis of 1 μm of diameter. The standards used were: Na on omphacite, Mg on olivine, Al-Si-Ca on grossular, Ti on ilmenite, Mn on rhodonite, Fe on fayalite, K on K-feldspar, Cr on metallic/pure Cr, Ni on niccolite and Sr on celestine. The WDS spectrometers used were TAP (for Na, Mg, Al, Si), PET-J (for Sr, Ti, Cr), LIFH (for Mn, Fe, Ni) and PETH (for K and Ca). The detection limit for these analyses is 0.01 wt% for each element.

Raman spectra of serpentines and carbonates were obtained at the Dipartimento di Scienze della Terra, Ambiente e Vita, University of Genova (Italy) using an XploRA PLUS Horiba micro-Raman. We used a 532 nm laser with a nominal power of 100 mW focused on the sample by a Olympus microscope with a 100× objective. The signal was dispersed using a 2400 g/mm grating and analyzed using a CCD detector. Raman spectra were collected in the spectral ranges 150–1150 and 3600–3800 cm^{-1}, corresponding to the vibration regions of the alumino-silicate network and of the O—H bond stretching, respectively. The calibration of the spectrometer was checked with a silicon wafer at 520.5 cm^{-1}.

Carbon and O isotope composition of carbonates were analyzed at the Department of Earth and Environmental Sciences, Lehigh University (USA), using a Finnigan MAT252 gas mass-spectrometer coupled with a GasBench II carrier gas system, applying the methods described in Collins et al. (2015). For this work, carbonates from different textural settings were sampled by micro-drilling using tungsten carbide bits with diameters of 1 or 2 mm. Following the methods of McCrea (1950), Paul and Skrzypek (2007), and Sharma et al. (2002), carbonate powder was reacted at 72 °C for 30 min (calcite), 3 h (dolomite) or 6 h (magnesite), with 0.2 ml 100% phosphoric acid (H_3PO_4), in order to release CO_2. All data presented here are reported in standard delta(δ)-notation (in permil – ‰), relative to VSMOW and VPDB for $\delta^{18}O$ and $\delta^{13}C$, respectively. Routine analyses of the international standard NBS-19 and of an in-house calcite standard allowed monitoring and correction of the data, resulting in a standard deviation (1σ) of 0.15‰ for both $\delta^{18}O$ and $\delta^{13}C$.

Strontium isotope analyses of several carbonate micro-drilled powders were performed using a Finnigan MAT 262 thermal ionization multicollector mass spectrometer, operated in dynamic mode (at IGG-CNR, Pisa, Italy). Carbonates were dissolved in HCl and, after complete drying, Sr was purified in an HCl solution using ion-exchange chromatography columns. Measured $^{87}Sr/^{86}Sr$ ratios were corrected for mass fractionation using $^{86}Sr/^{88}Sr = 0.1194$. During the analytical procedure, the Sr standard NIST SRM 987 ($SrCO_3$) yielded average values of $^{87}Sr/^{86}Sr = 0.710207 \pm 13$ (2σ, $n = 5$). Published values are adjusted to $^{87}Sr/^{86}Sr = 0.710250$. Strontium blanks were below 0.3 ng, negligible given the Sr concentration in carbonates. Because it is well known from the literature that carbonates have low Rb/Sr (*e.g.*, Cannaò et al., 2020), age corrections should not significantly affect the final $^{87}Sr/^{86}Sr$ values of the carbonates. For this reason and due to the high Sr content measured by EMPA in the carbonates that were analyzed (see Table 2), age-corrections were not applied.

3.2. Thermodynamic modeling

Pseudosection modeling was performed on select samples using the free energy minimization software Perple_X (v. 6.9.1; Connolly, 2005) in the system SiO_2-Al_2O_3-FeO-Fe_2O_3-MgO-CaO-K_2O-Na_2O-MnO, with H_2O at saturation. Solution models employed were those of: White et al. (2014) for chlorite, chloritoid, garnet, and mica; Green et al. (2007) for omphacite; and Holland and Powell (2011) for carpholite. Fluid was modeled using the Holland and Powell (1991) CORK equation of state assuming a pure H_2O fluid. Pseudosection modeling performed with a mixed H_2O-CO_2 fluid indicated the stabilization of a minimum of 6 vol% carbonate within the bulk assemblage over the modeled *P-T* range. Since we observe no carbonate within the modeled metapelite, we opted for a model with pure H_2O at saturation. Bulk-rock composition is based on thin section estimates of mineral abundance paired with microprobe analyses. A Fe^{3+}/Fe^{2+} value of 0.2 was used for the calculation as this value best reflects the average value within metamorphosed sedimentary rocks (c.f. Forshaw and Pattison, 2021). Pressure-temperature estimates are based on mineral assemblage, garnet composition isopleths, and the Si-in-phengite barometer (Massonne and Schreyer, 1989). Pseudosection results and *P-T* estimates are shown in Fig. 10.

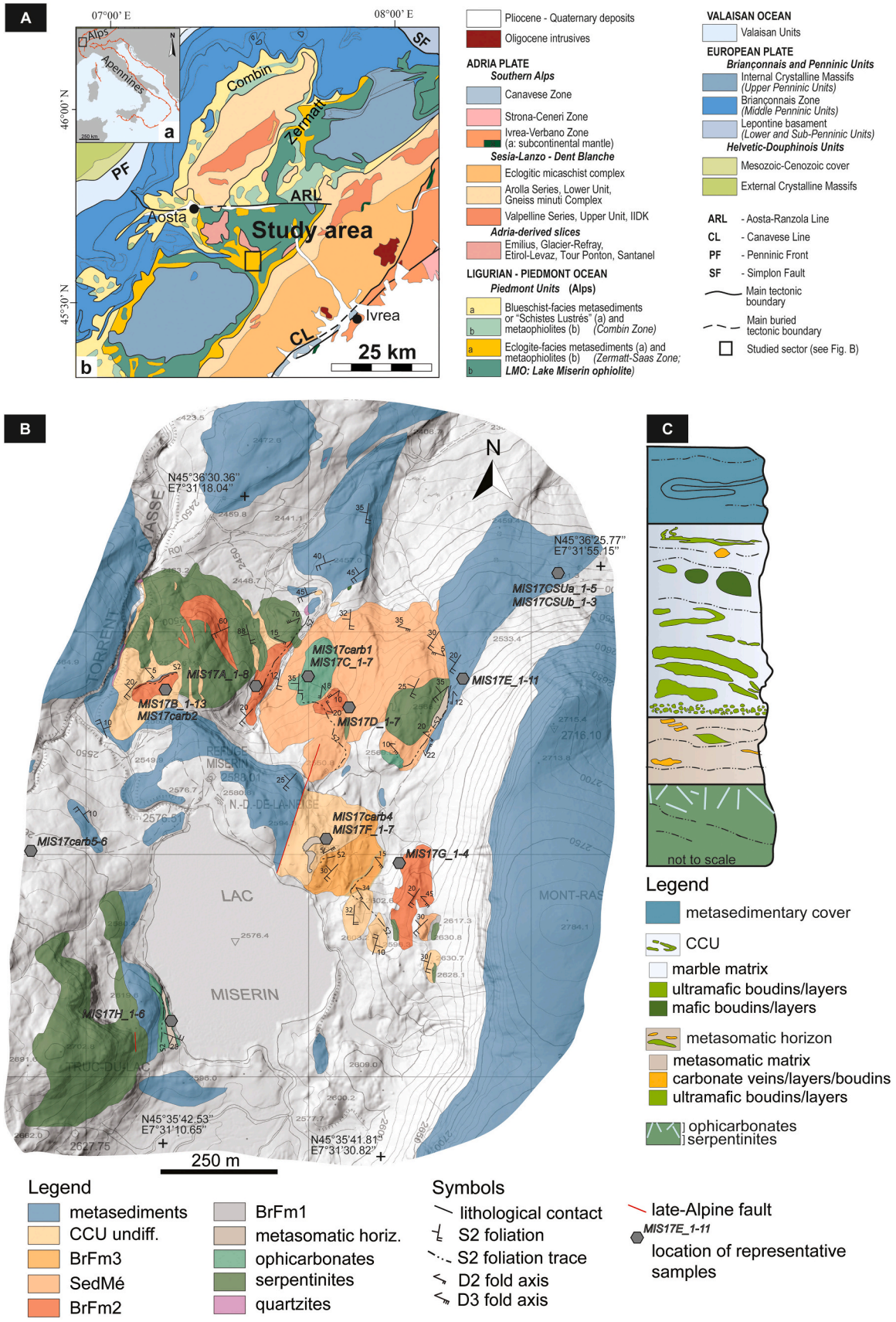

Fig. 1. (A) Tectonic map of the Western Alps with location of the study area (modified after Tartarotti et al., 2017). (B) Geologic map of the Champorcher metaophiolite with indication of the samples described in the text. (C) Simplified complete lithostratigraphic columnar section showing the relationships between the units comprising the metaophiolite sequence.

4. Field relations

From bottom to top, the metaophiolite sequence from the high Champorcher valley consists of a serpentinite basement, the composite chaotic unit (CCU) and a metasedimentary calcschist-dominated unit (CSU; Figs. 1B, C).

The basal serpentinite possesses both foliated and massive structures and grades into ophicarbonates, the latter which are either in contact with the overlying CCU or are separated from it by a cm- to m-thick metasomatic layer of carbonates (mostly dolomite and calcite) and green amphibole (Rotondo et al., 2021). Ophicarbonates are common in the high Champorcher Valley (Fig. 2A) and form discontinuous layers and blocks of variable size showing calcite-, dolomite- and locally magnesite-bearing vein networks several mm to cm thick (< 5 cm; Figs. 2A, B, C).

The CCU unit is up to 40 m thick and consists of clasts and blocks of ultramafic rocks in a foliated carbonate matrix (Fig. 2D) (Tartarotti et al., 2017): it includes several layers of both matrix- and clast-supported carbonate rocks whose fabrics resemble those of broken formations (Festa et al., 2010; Tartarotti et al., 2017). The CCU layers locally interfinger with a sedimentary mélange (Festa et al., 2010, 2019) consisting of a carbonaceous metasedimentary matrix with large serpentinite and mafic blocks. The CCU ultramafic fragments range in size from millimetric-centimetric pebbles in the basal part to metric-decametric blocks towards the top of the unit. A key feature is the occurrence of metamorphic carbonate-bearing veins in the serpentinite blocks embedded in the CCU and in the interfingered mélange. Such veins are either several cm thick and filled by carbonate ± fibrous serpentine (Fig. 2C) or occur as dolomite + chlorite + diopside ± tremolite tensional veins in-between boudinaged ultramafic CCU blocks (Fig. 2D, E) displaced parallel to the stretching direction of the main S_2 regional foliation (see below). Comparable dolomite + chlorite + diopside veins up to 20 cm thick and several m long (Fig. 2F) cut the largest serpentinite blocks in the broken formation and in the mélange.

The CSU calcschist unit is composed of layered, carbonate-rich flysch-like rocks (*i.e.,* calcschists) devoid of ophiolitic detrital material interbedded with quartz-garnet-chloritoid-bearing micaschists. The latter are characterized by abundant pseudomorphs after lawsonite porphyroblasts marking a well-developed foliation (Fig. 2G; S_2, see below). The metasedimentary unit overlying the CCU can also be in

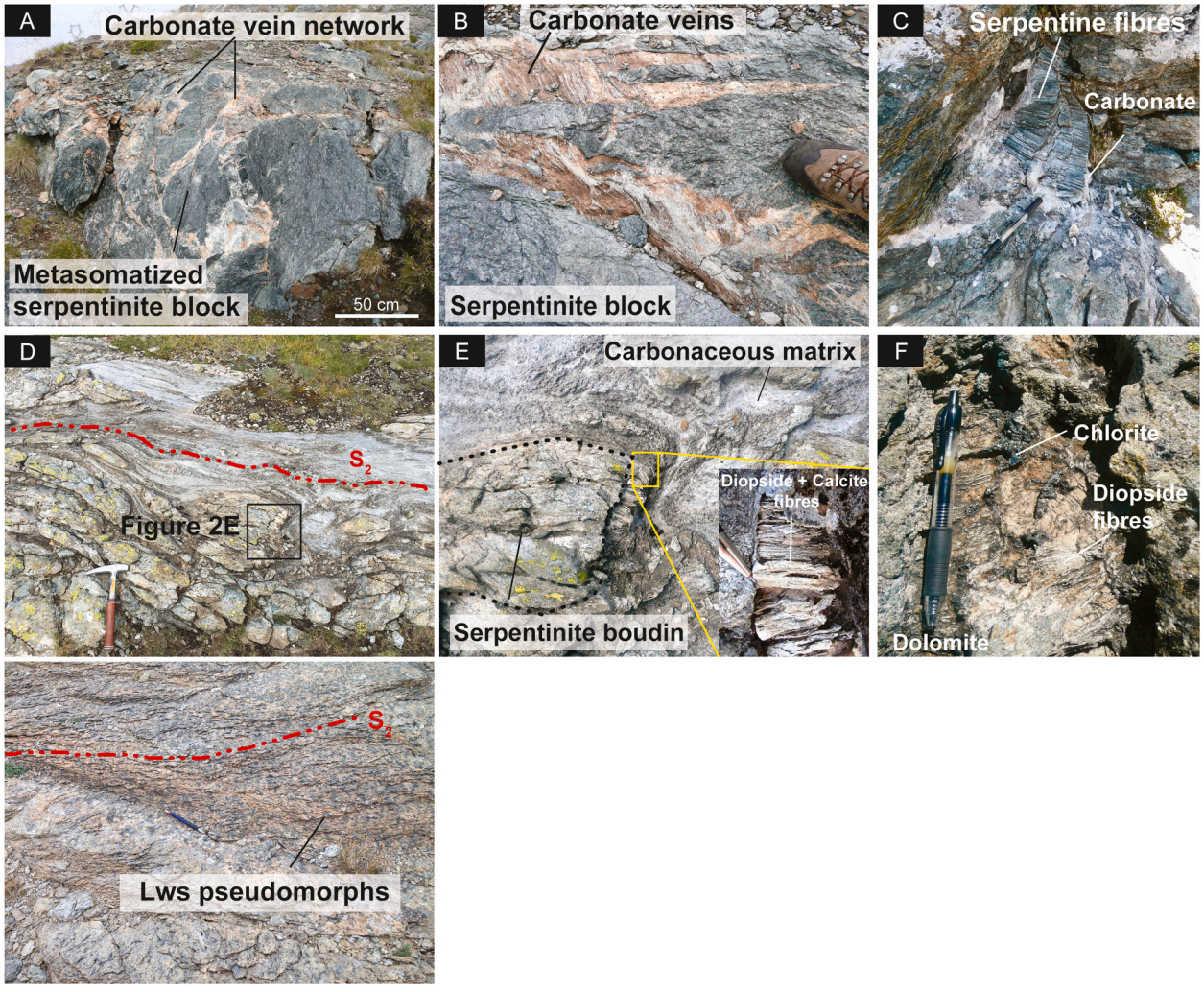

Fig. 2. Field images of the Champorcher lithologies. (A), (B) Ophicarbonates showing blocks of metasomatized serpentinites, *i.e.* chlorite-schists, dominated by chlorite + amphibole (tremolite-actinolite series) ± epidote ± magnetite ± talc, with a diffused network of veins, filled with carbonate minerals (calcite, dolomite and magnesite). (C) Carbonate and fibrous serpentine cm-thick veins interfingered among ultramafic clasts within the CCU. (D) CCU ultramafic clasts dismembered and boudinaged along S_2 foliation. Boudins are enveloped by carbonaceous matrix. In the inset a boudin with veins filling the boudin neck is highlighted. (E) Detail of a boudin neck characterized by vein infill consisting of fibres of diopside and carbonates growing parallel to S_2 stretching direction (see inset for details). (F) Dolomite, diopside and chlorite bearing vein crosscutting serpentinites. The vein reaches 30 cm in thickness and over 2 m in length. (G) Lawsonite pseudomorphs aligned along S_2 foliation planes in calcschists.

direct contact with serpentinites showing a sharp basal contact that may correspond to an inherited oceanic depositional surface. However, Alpine tectonics intensely reworked the pristine oceanic structures.

The contacts between calcareous metasediments and serpentinites are frequently marked by the occurrence of metasomatic horizons, interfingered between the two rock types. These horizons are widespread and occur between: (i) the serpentinite basement and the CCU, (ii) serpentinite blocks and the surrounding calcareous matrix within the CCU; (iii) large ultramafic blocks and the overlying CSU calcschist. The metasomatic horizons consist of light green to dark green layers of amphibole (actinolite-tremolite) + chlorite + epidote + serpentine, alternating with orange-coloured carbonate-rich layers (*e.g.,* Rotondo et al., 2021) developing a foliation parallel to the main regional schistosity (see below). The associated serpentinite blocks show increased carbonate vein networks and the occurrence of large metamorphic veins containing dolomite + diopside + chlorite.

The Champorcher metaophiolite records a polyphase ductile deformation evolution as summarized in Fig. 3. An early D1 schistosity (S_1) overprints the sedimentary bedding (S_0) in the top calcschist sequence, but it is poorly preserved in the CCU chaotic unit. In the CSU calcschists, the high-*P*/low-*T* assemblage marking the S_1 is rarely preserved due to overprinting during subsequent recrystallization. The S_1 schistosity in calcschists is deformed by isoclinal D2 folds developing a S_2 axial plane foliation that represents the regional foliation in the Champorcher area (Fig. 1B). In calcschists and micaschists, S_2 is marked by garnet, phengite, zoisite and chloritoid; also present are lozenge-shaped pseudomorphs of zoisite + albite + paragonite after lawsonite porphyroblasts associated with the S_2. In the CCU, S_2 is marked by serpentine + amphibole+ diopside + chlorite+ carbonates + epidote + magnetite± talc. S_1 and S_2 thus relate to the prograde to peak subduction path of the Champorcher rock package.

All contacts between the different CCU units are parallel to each other and to the main S_2 foliation: the occurrence of boudinaged blocks parallel to S_2 foliation in the different CCU subunits and of boudinaged D2 fold limbs attest to a shear component during D1 and D2 deformation. A late deformation stage (D3) locally caused crenulation of the above structures without development of new foliations (Fig. 3). Overall, the CCU block-in-matrix fabric likely derives from the superposition of Alpine deformation onto sedimentary features acquired in the Jurassic Tethys.

5. Petrography and microstructures

Here we describe the key petrographic features of the samples aimed at demonstrating the correspondence between mineralogical assemblages and relative textures to constrain the metamorphic reactions involving C-bearing fluids responsible for carbonation and decarbonation reactions during prograde metamorphism.

5.1. *Basal serpentinites and ophicarbonates*

The ultramafic rocks from Champorcher are in many ways similar to other Alpine serpentinites and ophicarbonates (Li et al., 2004). The massive varieties preserve rare crystals of porphyroclastic mantle clinopyroxene and display pseudomorphic replacements of mantle minerals: pyroxenes were mostly serpentinized, mesh serpentine textures developed after mantle olivine; magnetite rimmed by chlorite and serpentine likely replaced mantle spinel. In massive rocks, serpentine can be overgrown by sub-millimetric to millimetric carbonate patches. Deformed serpentinites display a serpentine + pyroxene + tremolite +

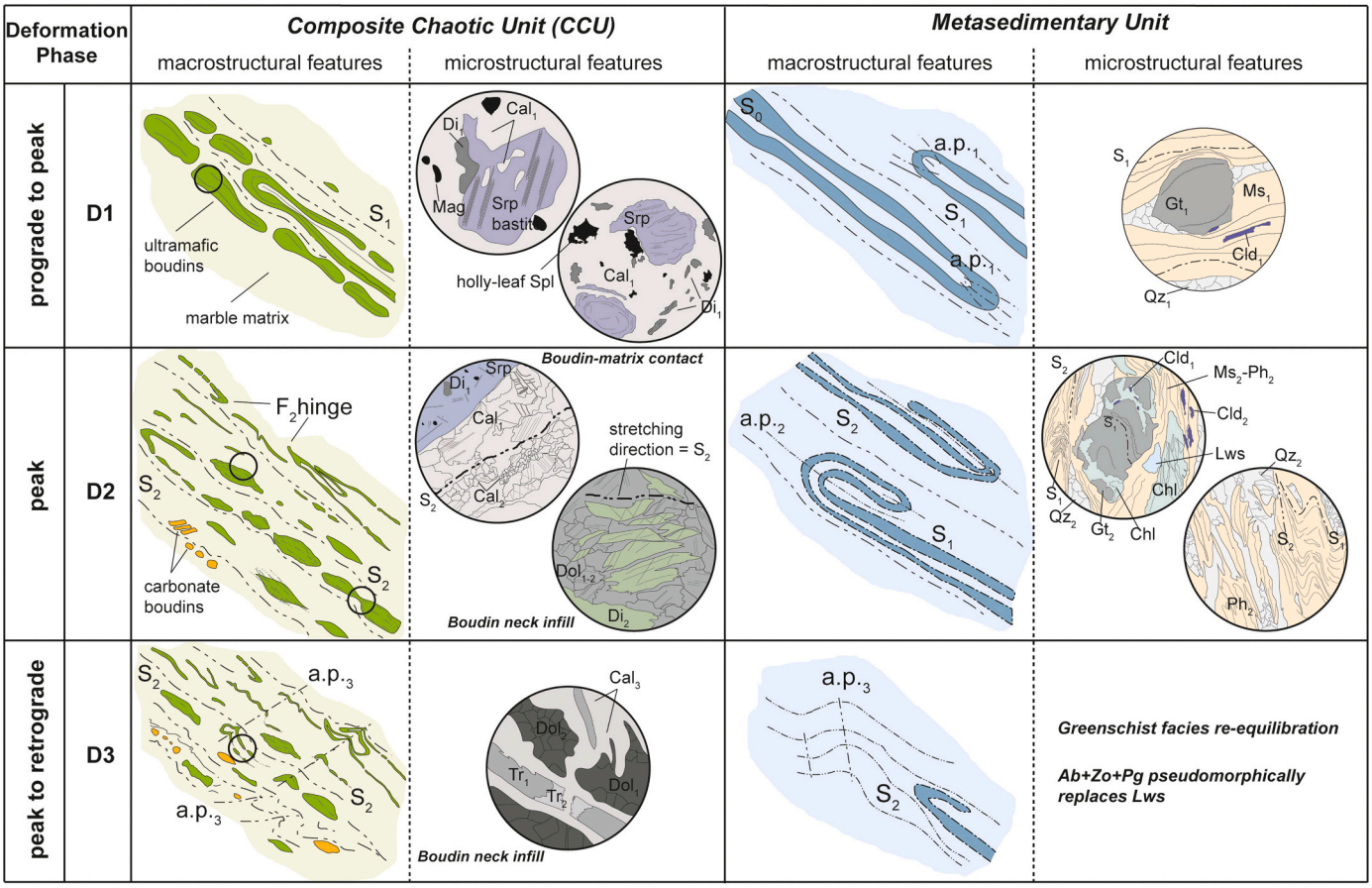

Fig. 3. Mesostructures and microstructures revealing the tectono-metamorphic history of the CCU and CSU. For each recognized deformation phase the representative structures and mineralogical assemblage are schematically reported.

chlorite ± opaque foliation. An interesting feature is represented by the occurrence of dolomite + magnesite aggregates transposed along the main alpine S_2 serpentinite foliation. In such aggregates, fine-grained dolomite replaces former coarse-grained magnesite. Ophicarbonates consist of serpentine (Srp) + chlorite (Chl) + tremolite (Tr) ± epidote (Ep) ± magnetite (Mt) ± talc (Tlc); the veins contain calcite, dolomite (Dol) and locally magnesite (Fig. 2A). In all basal serpentinite and ophicarbonate samples, no metamorphic olivine has been detected and antigorite is the main serpentine type identified by Raman spectroscopy.

5.2. CCU matrix and ultramafic clasts

Petrography of the CCU clasts and matrix allows insights regarding the reactive structures and attests to the carbonation and decarbonation processes having occurred during D1 to D3 deformation. The earliest D1 stage caused stretching and transposition of serpentinite clasts, diffuse serpentinization of mantle minerals and calcite/dolomite growth after serpentine replacements of mantle minerals. The D2 peak metamorphic stage further enhanced transposition and boudinage of the serpentinite clasts and, within the carbonate matrix, caused crystallization of neoblastic calcite and dolomite stable with minor *syn*-tectonic serpentine (Fig. 3). The D3 retrograde stage caused crenulation of pre-existing structures and crystallization of new, late stage, calcite replacing earlier-crystallized calcite and dolomite grains (Fig. 3).

5.2.1. Ultramafic clasts

The CCU ultramafic clasts (*e.g.*, MS17A_1 sample, see Fig. 2D) are stretched and transposed along the main S_2 foliation developed in the carbonate matrix (*e.g.,* A2 sample, see Fig. 2D) and consist of serpentine (~35%), calcite (Cal, ~50%), diopside (Di, ~10%) and opaque (Opq, ~5%) displaying a brecciated microtexture.

Based on the results of Rotondo et al. (2021) and on Raman checks performed on our samples antigorite is the most abundant serpentine phase in these clasts. Mantle orthopyoxene and olivine are fully replaced by antigorite serpentine ± magnetite; mantle clinopyroxene is replaced by antigorite and neoblastic diopside (Di_2), and primary mantle

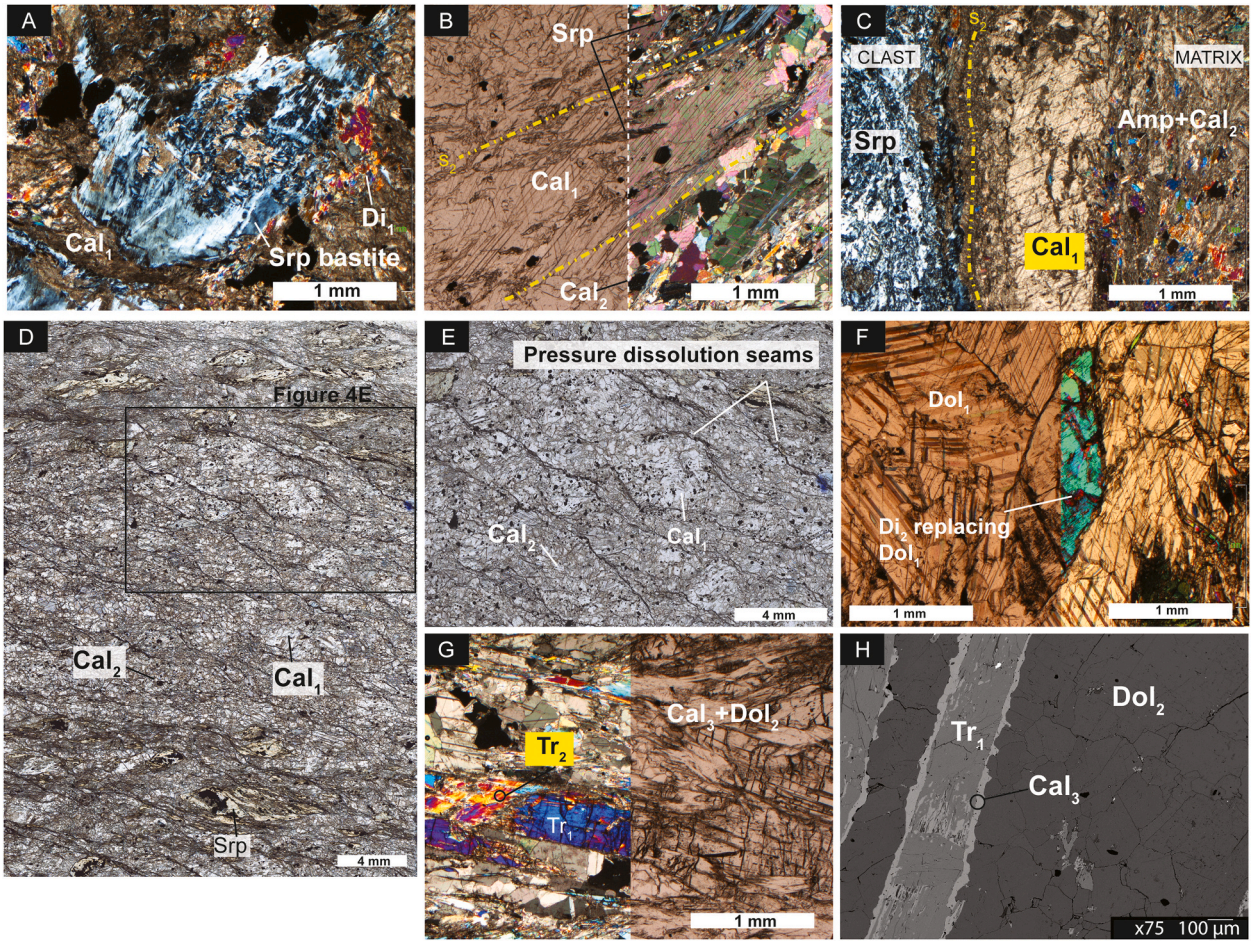

Fig. 4. Petrography of the Champorcher Composite Chaotic Unit (CCU). Images from A to C are representative of the carbonation process (Mg-Ol + Ca-Py(Di_1) + $2CO_2 + 2H_2O$ ➔ Srp + Cal_1 + Mgs) responsible for the crystallization of carbonates at the expenses of serpentinite-forming silicates. (A) Detail of an ultramafic clast with Srp bastite (likely replacing former Opx) and Di_1 overgrown by crypto-crystalline Cal_1 attesting for carbonation process. (B) Detail of the CCU matrix with Cal_1 porphyroclast elongated parallel to S_2 foliation planes and displaying Cal_2 neoblasts along its grain boundaries. Srp fibres display a shape preferred orientation marking S_2 planes. Left portion of the image: plane polarised light; right portion of the image: cross polarised light. (C) Contact between a Srp-bearing clast and carbonaceous matrix within the CCU. In the matrix (middle to right portion of the image) Cal_1 porphyroclast is elongated parallel to S_2 foliation and is dynamically recrystallized in Cal_2 small-grained aggregates associated with Amp along S_2 planes. Cross polarised light. (D) Closely spaced stylolite inside the carbonate-rich matrix of the CCU. (E) Detail of the stylolite in fig. D. (F) Detail of Di_2 pseudomorphically growing on former Dol_1 attesting for the decarbonation process (Dol_1 + $SiO_{2,aq}$ ➔ Di_2 + CO_2) causing the growth of silicates at the expense of former carbonates. Left portion of the image: plane polarised light; right portion of the image: cross polarised light. (G) Extensional high-*P* veins formed in the boudin neck with Tr_2 and interstitial Cal_3 growing at the expenses of former carbonates (Dol_2 and Dol_1) and silicates (Di_2 and Tr_1). These textural relationships attest for a secondary carbonation process (Tr_1/Di_2 + $Dol_{1/2}$ + fluids ➔ (Atg) + Cal_3 + Tr_2) occurring after previous decarbonation. Left portion of the image: plane polarised light; right portion of the image: cross polarised light. (H) Back-scattered electron image (BSE) of a portion of extensional vein with Cal_3 interstitial to Tr_1 and Dol_2 crystals.

clinopyroxene (Di_1) rarely occurs as fine-grained relics (Fig. 3).

Serpentine and diopside are overgrown by micro- to cryptocrystalline dusty-brownish calcite without any apparent structural control (Fig. 4A). Calcite displays abundant inclusions of serpentine fibres wrapping around the ultramafic domains. Despite the intense carbonation (70–80% in volume), some sites still retain early stage (pre—D_1?) textures such as holly-leaf spinel texture and bastite serpentine (Figs. 3, 4A).

The several metres-long Dol + Di + Chl veins cutting the largest serpentinite bodies (Fig. 2F) are very similar in mineralogy and composition to the extensional veins described above. In these larger veins, calcite replaces coarse dolomite coexisting with cm-scale fibrous diopside, chlorite and opaques (*i.e.,* Cal_3, commonly interstitial to diopside).

5.2.2. CCU matrix and high-P veins

The CCU matrix envelops ultramafic clasts and consists of $Cal_{1,2}$ (80%), Srp (10%), Di (5%), Opq (2%), clinozoisite (Czo) (<3%) forming a foliated texture with inequigranular aggregates of $calcite_{1,2}$ alternating with irregular serpentine layers (Fig. 3). Millimeter-sized $calcite_1$ porphyroclasts with deformation twins derive from carbonation of ultramafic clasts and are dynamically recrystallized to $calcite_2$ neoblasts synkynematic with S_2 development (see Figs. 3, 4B, C). These latter consist of strain-free porphyroblasts occurring in equigranular fine- to medium-grained aggregates with polygonal boundaries aligned to define S_2 foliation planes (Fig. 4B). The S_2 foliation planes are discontinuously marked by the shape and preferred orientation of serpentine fibrous aggregates, which were passively rotated parallel to foliation planes (Fig. 3, Fig. 4B).

The occurrence of closely spaced pressure solution seams parallel to S_2 is a key feature of most samples in the carbonate-rich matrix of the CCU (Fig. 4D). The pressure solution structures are grossly parallel to the main S_2 foliation and involve all types of carbonate crystals (Figs. 4D, E). Carbonates contacting the pressure solution seams display varying shapes, from irregular and indented with nearby grains, to flattened (Figs. 4D). The pressure solution planes are black in colour: based on micro-Raman investigations no graphite has been found in such planes, but abundant micrometric to millimetric diopside and tremolite (Tr) have been observed replacing the carbonate minerals.

While the ultramafic clasts in the CCU display carbonation of the rock-forming silicates (Figs. 4A, C), the necks between the boudinaged ultramafic clasts retain evidence of decarbonation reactions. This is evidenced by silicate minerals overgrowing carbonates (Fig. 3, Fig. 4F, G). In particular, the decarbonation reactions in boudins and boudin necks resulted in pseudomorphic growth of Di_2 on former Dol_1 (Fig. 4F). The crystallization of Tr_1 and Di_2 oriented parallel to the S_2 stretching direction (Fig. 4G), and along the pressure dissolution planes, link the decarbonation processes to the prograde history of the Champorcher rocks.

The mobilization of C-bearing fluids during the decarbonation reactions is supported by silicate- and carbonate-bearing extensional veins formed in the necks between the ultramafic boudins (*e.g.,* A3A sample, see Figs. 2E, 4F, G) and containing Dol (45–25%), Di (35–25%), Chl (5–10%), actinolite-tremolite (Act-Tr 5–35%), Opq (<5%), Cal_3 (15%). These veins display diopside and/or amphibole fibres growing parallel to the S_2 foliation and to the main stretching direction (Fig. 3).

Subsequent carbonation processes locally occurred as interstitial calcite overgrowing either silicates or prograde dolomite (Figs. 4H). This late-stage process likely occurred during the retrograde D3 event(s).

5.2.3. Metasomatic reaction rinds

The metasomatic reaction rims show a range of textures, from brecciated to foliated. They generally occur between the carbonate matrix of the CCU and the embedded serpentinite clasts; the mineral assemblage is generally the same, though with different modal abundances: dolomite, calcite, tremolite, chlorite, diopside, talc (Tlc), opaque minerals, serpentine. Samples collected along a 3 m-long profile from the carbonate rock matrix to a serpentinite block show transition from (1) a carbonate-rich rock comparable to the one presented in Figs. 4B, C, to (2) a carbonate-bearing rock containing increasing abundance of silicate minerals like amphibole and clinopyroxene (Fig. 5A, B), to a variably carbonated serpentinite (Fig. 5C). Raman spectroscopy of serpentine in such carbonated ultramafic rocks shows that it is antigorite, the serpentine phase stable under high-*P/T* conditions (Fig. 5D, E). In such profiles of metasomatic zone, the carbonate-bearing rocks show increasing replacement of dolomite and calcite by silicate minerals, along pressure solution surfaces (Fig. 4D, E), the main foliation and in patches: Fig. 5A shows the static development of tremolite, diopside and minor chlorite at the expense of pre-existing carbonates. This rock type then passes to the metasomatic horizon, where diopside and tremolite become dominant. In contrast, the associated nearby serpentinite records development of carbonate patches and networks of mm- to cm-sized carbonate veins cross-cutting and overgrowing the antigorite matrix (Fig. 5C).

5.3. Metasedimentary cover – Micaschists and calcschists

Quartz-rich micaschists (sample CSA5) consist mostly of Qz (40%), white micas (muscovite-phengite-paragonite – 30%), Chl (15%), garnet (Grt, 10%), Opq (5%). Accessory epidote (allanite-zoisite-clinozoisite - 3-5%), tourmaline (Tur <3%), $chloritoid_{1,2}$ (Cld, 3%) are also present. In micaschists, remnants of an early S_1 foliation are preserved within the regional, high-*P* S_2 foliation. While S_1 is marked by a generation of Si-poor white mica (Wm_1), Grt_1, Cld_1, Qz_1, and Opq, (Fig. 3, Fig. 6A), the peak metamorphic assemblage along S_2 consists of Si-rich phengitic white mica (Wm_2) + lawsonite (Law) + Cld_2 + Chl + Aln epidote (Fig. 3, Figs. 6A, B, C).

$Grt_{1,2}$ is wrapped by the S_2 foliation and retains an internal S_1 foliation (oblique to S_2) marked by Cld_1, Wm_1 and Qz inclusions (Fig. 3, Fig. 6). Based on the relationship between the external S_2 foliation and the S_1 preserved in garnet, Grt growth is pre- to *syn*-kynematic with respect to the D2 deformation stage. Remarkably, aggregates (up to 3–4 cm in size) with orthorhombic shape and composed of albite + epidote + paragonitic white $mica_3$ occur within the S_1-S_2 foliations. Such aggregates are interpreted as pseudomorphs after lawsonite (Fig. 3). D3-related pseudomorphs on former lozenge-shaped Lws crystals are visible along cleavage planes (Fig. 3).

Overall, structures associated with the D2 stage are the most penetrative also within the metasedimentary cover and are associated with the peak metamorphic conditions (high-*P* subduction event) as indicated by syn-kynematic aggregates of Grt_2, Cld_2 and Ph_2 along S_2 foliation planes.

6. Mineral chemistry

Tables 1 and 2 present representative major element compositions of carbonates and silicates from the CCU and from the micaschist sample CSA5.

6.1. Carbonates from the CCU

The composition of the different generations of calcite within the CCU is relatively homogeneous but with some noteworthy variations. In particular, $calcite_1$ replacing serpentine in clasts or from the carbonate matrix show variable enrichment in MgO from 0.42 to 1.38 wt% and limited amounts of FeO ranging between 0.11 and 0.24 wt%. The SrO content of $calcite_1$ from the CCU matrix can be up to 0.13 wt%, while SrO in $calcite_1$ from the ultramafic clasts is below detection (< 0.01 wt %). Recrystallized $calcite_2$ in the CCU matrix is similar in composition to $calcite_1$. Late-stage $calcite_3$ replacing dolomite and/or silicates is variably Mg- and Fe-rich, up to 0.94 and 0.20 wt%, respectively. Dolomite in the high-*P* veins shows Ca/Mg of 1.3–1.4 and is particularly enriched

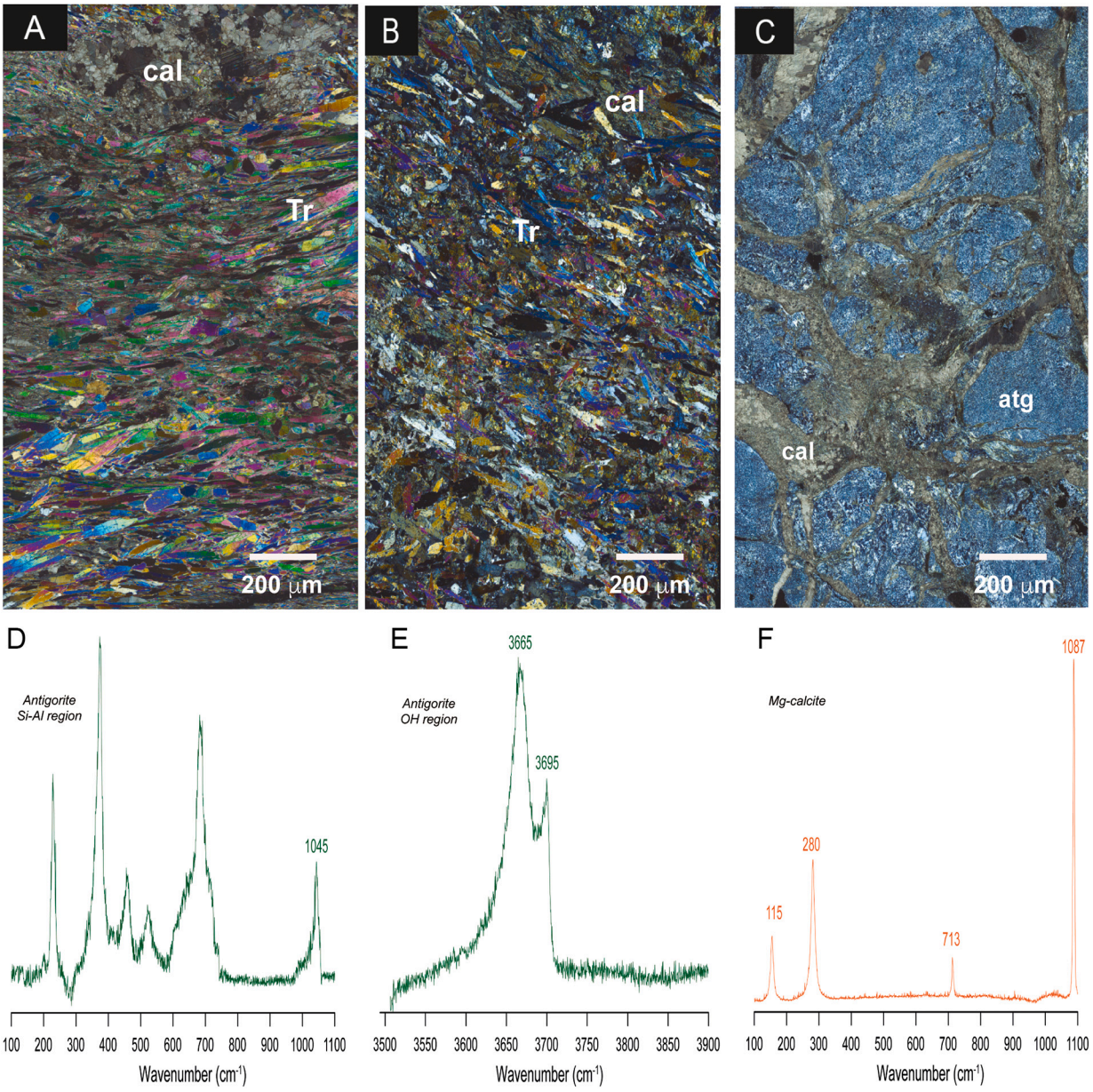

Fig. 5. (A), (B) Carbonate-bearing rocks containing increasing abundance of silicate minerals like amphibole and clinopyroxene. In plate A, the central and lower part of the figure consist of tremolite, while the upper part is made of carbonate overgrown by tremolite. (C) Variably carbonated serpentinite showing networks of millimetric to centimetric carbonate veins cutting and overgrowing the serpentine matrix. (D), (E) Different regions of the Raman spectra of antigorite serpentine from the ophicarbonate sample reported in plate (C). (F) Raman spectrum of Mg-calcite.

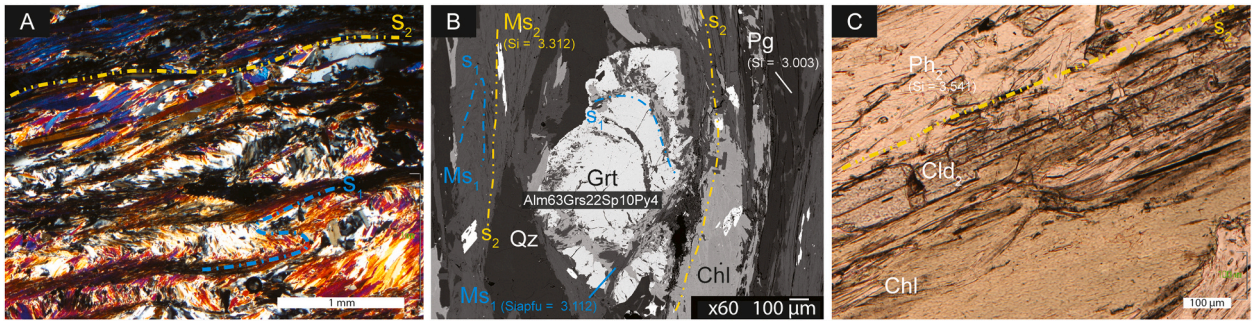

Fig. 6. Petrography of the Champorcher metasedimentary cover. (A) Crenulation cleavage defined by S_1 fold hinges transposed along S_2 cleavage planes. Crossed polarised light. (B) Grt porphyroblast enveloped by S_2 foliation marked by Ms_2, Pg_2, Qz, Chl. S_1 foliation inside Grt is marked Wm_1, Cld_1, Qz_1. (C) S_2 foliation marked by Ph_2 mica, Chl and Cld. Plane polarised light.

Table 1
Mineral chemistry of representative rock-forming minerals of the CCU.

	Carbonates										Clinopyroxene		Amphibole		Serpentine			
Sample	A1	A2	A2	A3A	A3A	CRB5	A3A	A3A	A3A	A3A	A1	A3A	A3A	A1	A1	A1	A2	A3A
Unit	BrFm2. Clast	BrFm2 Matrix	BrFm2 Matrix	BrFm2 Vein	BrFm2 Vein	BrFm1 Matrix-clast contact	BrFm2 Vein	BrFm2 Vein	BrFm2 Vein	BrFm2 Vein	BrFm2 Clast	BrFm2 Vein	BrFm2 Vein	BrFm2 Clast	BrFm2 Clast	BrFm2 Clast	BrFm2 Matrix	BrFm2 Vein
Texture	Cal1 on Srp	Cal1	Cal2	Cal3	Cal3	Cal2 sinS2	Dol1	Dol1	Dol2	Dol2	Di in Cal3	Di core	Tr	Tr	Srp fibres in Cal3	Srp	Srp in Cal2	Srp in Cal3
SiO_2	0.07	<0.01	0.01	0.01	0.05	0.04	<0.01	<0.01	0.01	0.01	55.00	55.59	59.00	58.35	41.58	40.59	43.10	44.03
TiO_2	<0.01	0.02	0.05	0.03	0.02	0.05	<0.01	<0.01	0.05	0.01	<0.01	0.09	0.01	<0.01	0.02	<0.01	<0.01	0.02
Al_2O_3	<0.01	<0.01	0.02	<0.01	<0.01	0.01	0.01	<0.01	0.01	<0.01	0.06	0.02	0.09	0.12	1.98	3.20	1.26	0.94
Cr_2O_3	0.02	0.03	0.01	<0.01	0.04	<0.01	<0.01	<0.01	0.01	<0.01	0.11	<0.01	0.09	0.16	0.62	1.31	0.01	0.16
FeO	0.24	0.11	0.14	0.16	0.12	0.05	1.37	1.29	1.28	1.11	1.17	1.47	1.21	1.14	3.83	3.87	3.70	2.98
MnO	0.10	0.00	0.06	0.21	0.07	0.07	0.19	0.17	0.26	0.12	0.07	0.04	0.09	0.04	0.08	0.06	0.01	0.04
MgO	1.38	0.42	0.94	0.36	0.31	0.00	22.46	22.62	23.22	23.88	17.94	17.26	23.81	23.81	36.31	35.38	36.55	37.61
CaO	55.63	57.99	56.83	39.71	50.85	45.14	32.94	32.81	32.33	32.06	24.54	25.83	13.67	13.55	0.10	0.03	0.17	0.13
Na_2O	0.00	0.06	0.02	0.02	0.02	0.03	<0.01	<0.01	0.04	0.01	0.14	0.12	0.04	0.03	0.04	<0.01	0.02	0.02
K_2O	<0.01	0.01	<0.01	0.01	0.01	0.01	<0.01	<0.01	<0.01	<0.01	<0.01	<0.01	0.02	0.02	<0.01	<0.01	<0.01	<0.01
SrO	<0.01	0.13	0.07	0.01	0.14	0.04	0.20	0.04	<0.01	<0.01	–	–	–	–	<0.01	<0.01	<0.01	<0.01
Total	57.44	58.75	58.15	40.51	51.64	45.43	57.17	56.94	57.22	57.22	99.17	100.49	98.14	97.51	85.02	84.9	85.23	86.05
Si	0.000	0.000	0.000	0.000	0.000	0.000	0.000	0.000	0.000	0.000	2.000	2.010	8.000	7.960	33.200	32.510	34.140	34.330
Ti	0.000	0.000	0.000	0.000	0.000	0.000	0.000	0.000	0.000	0.000	0.000	0.000	0.000	0.000	0.010	0.000	0.000	0.010
Al	0.000	0.000	0.000	0.000	0.000	0.000	0.000	0.000	0.000	0.000	0.000	0.000	0.010	0.020	1.860	3.020	1.180	0.870
Cr	0.000	0.000	0.000	0.000	0.000	0.000	0.000	0.000	0.000	0.000	0.000	0.000	0.010	0.020	0.390	0.830	0.010	0.100
Fe	0.010	0.000	0.000	0.010	0.000	0.000	0.030	0.030	0.030	0.030	0.040	0.050	0.140	0.100	2.560	2.590	2.450	1.940
Mg	0.070	0.020	0.050	0.030	0.020	0.000	0.950	0.960	0.980	1.000	0.980	0.930	4.810	4.840	43.200	42.240	43.140	43.700
Mn	0.000	0.000	0.000	0.010	0.000	0.000	0.010	0.000	0.010	0.000	0.000	0.000	0.010	0.000	0.050	0.040	0.010	0.030
Ca	1.920	1.970	1.950	1.960	1.970	1.990	1.000	1.000	0.980	0.970	0.960	1.000	1.990	1.980	0.090	0.030	0.150	0.110
Na	0.000	0.000	0.000	0.000	0.000	0.000	0.000	0.000	0.000	0.000	0.010	0.000	0.010	0.010	0.060	0.000	0.040	0.030
K	0.000	0.000	0.000	0.000	0.000	0.000	0.000	0.000	0.000	0.000	0.000	0.000	0.000	0.000	0.000	0.000	0.000	0.000
Sr	0.000	0.002	0.001	0.000	0.003	0.001	0.003	0.001	0.000	0.000	–	–	–	–	0.000	0.000	0.000	0.000

Cal: calcite; Dol: dolomite; Di: diopside; Tr: tremolite; Srp: serpentine.

Table 2
Mineral chemistry of representative rock-forming minerals in micaschist sample CSA5.

	Garnet (Grt)						White mica (Wm)						Chlorite		Chloritoid	
Texture	Grt core	Grt rim	Grt core	Grt core	Grt rim	Grt core	Wm 1 incl in garnet	Wm 2	Wm 2	Wm 2	Wm 2	Wm 3 paragonite	incl in garnet	S2	incl in garnet	S2
SiO_2	37.55	37.00	37.39	37.70	38.20	38.10	47.89	53.47	50.27	52.52	53.00	47.68	24.45	23.98	24.56	24.26
TiO_2	0.04	0.06	0.02	0.12	0.09	0.04	0.15	0.13	0.27	0.15	0.19	0.09	0.03	0.09	<0.01	<0.01
Al_2O_3	21.56	21.31	21.86	21.95	21.71	21.75	36.50	25.78	30.42	27.29	27.08	40.60	23.41	22.60	41.20	41.26
Cr_2O_3	0.10	0.09	0.06	0.03	0.06	0.02	0.03	<0.01	0.06	<0.01	0.08	<0.01	0.02	0.00	0.05	0.01
FeO	28.93	28.92	27.45	28.13	27.79	27.68	1.46	2.47	3.16	3.25	3.08	0.34	30.28	30.48	24.63	25.23
MgO	1.02	0.70	1.03	1.03	1.04	0.93	0.57	3.36	2.18	3.15	3.11	0.15	11.08	10.01	0.57	1.70
MnO	4.52	4.78	8.34	4.12	3.52	4.87	0.09	0.04	<0.01	0.04	0.03	<0.01	0.32	0.36	2.26	1.44
CaO	8.05	7.59	5.42	8.68	10.00	9.01	0.04	<0.01	0.02	<0.01	<0.01	0.07	0.02	0.02	0.01	0.01
Na_2O	<0.01	<0.01	<0.01	<0.01	<0.01	<0.01	0.83	0.08	0.43	0.12	0.32	6.61	0.03	0.01	0.01	0.02
K_2O	<0.01	<0.01	<0.01	<0.01	<0.01	<0.01	8.95	9.66	9.15	9.57	8.89	0.61	0.02	0.01	0.01	<0.01
Total	101.77	100.45	101.57	101.76	102.41	102.40	96.51	94.99	95.96	96.09	95.78	96.15	89.66	87.56	93.30	93.93
Si	2.971	2.973	2.966	2.966	2.987	2.987	3.113	3.542	3.312	3.456	3.481	3.003	5.157	5.201	1.879	1.857
Ti	0.002	0.004	0.001	0.007	0.005	0.002	0.007	0.007	0.014	0.008	0.009	0.004	0.005	0.014	0.000	0.000
Al	2.011	2.018	2.049	2.039	2.001	2.010	2.796	2.013	2.362	2.116	2.097	3.014	5.829	5.791	3.978	3.992
Cr	0.006	0.006	0.004	0.002	0.003	0.001	0.002	0.000	0.003	0.000	0.004	0.000	0.004	0.000	0.003	0.000
Fe	19.500	19.270	19.730	19.780	19.590	19.590	0.080	0.137	0.174	0.179	0.169	0.018	21.090	20.340	1.576	1.615
Mg	0.120	0.083	0.122	0.121	0.121	0.109	0.055	0.332	0.214	0.309	0.305	0.014	3.483	3.236	0.258	0.165
Mn	0.303	0.325	0.560	0.275	0.233	0.323	0.005	0.003	0.000	0.002	0.002	0.000	0.057	0.066	0.037	0.110
Ca	0.682	0.653	0.461	0.732	0.838	0.757	0.003	0.000	0.001	0.000	0.000	0.005	0.005	0.004	0.001	0.001
Na	–	–	–	–	–	–	0.104	0.011	0.055	0.016	0.041	0.807	0.021	0.008	0.004	0.006
K	–	–	–	–	–	–	0.742	0.816	0.769	0.804	0.745	0.049	0.010	0.008	0.001	0.000
Almandine	63	64	61	62	60	60										
Andradite	0	0	0	0	0	0										
Grossular	22	22	15	25	28	25										
Pyrope	4	3	4	4	4	4										
Spessartine	10	11	19	9	8	11										
Uvarovite	0	0	0	0	0	0										

in FeO from 1.11 to 1.37 wt%. The SrO content of dolomite$_1$ can be up to 0.20 wt%, while it is below detection in dolomite$_2$.

6.2. Silicates within the CCU

Serpentine is generally poor in Fe with a Mg# ranging between 0.91 and 0.97 (Mg# = Mg/(Mg + Fe$_{tot}$)); it shows low Al_2O_3 (average 1.42 wt %), Cr_2O_3 (average 0.31 wt%) and NiO_2 (< 0.46 wt%).

Pyroxene has a homogeneous composition near that of the diopside end member (En = 49, Wo = 59, Fs = 2) while all amphiboles correspond to tremolite (Hawthorne et al., 2012). Based on Si and Fe^{2+} + Fe^{3+} contents, chlorite has a penninitic composition (Si = 6.494 c.p.f.u.).

6.3. Metasedimentary cover (CSU)

The micaschist sample CSA5 displays high-*P* mineralogical assemblages marking both D1 and D2-related structures. White mica$_2$ marking S_2 foliation is a Si-rich phengite (Si from 3.456 to 3.542 c.p.f.u.; Fig. 6), whereas white mica$_1$ inclusions in garnet and the paragonitic white mica$_3$ show lower Si than the phengitic Wm$_2$ (Si from 3.113 and 3.003 c.p.f.u.; Table 2 and Fig. 6B). Chlorite has a ripidolitic composition (Si = 5.2 c.p.f.u.). Garnet porphyroblasts are almandine-rich and do not show significant variations between D1-related cores (Grt$_1$) and D2-recrystallysed rims (Grt$_2$) displaying comparable and appreciable amounts of grossular molecule followed by spessartine and pyrope ($Alm_{63}Grs_{22}Sp_{10}Py_4$). Chloritoid (Cld$_1$) included in Grt$_1$ cores is richer in MgO than Cld$_2$ marking the S_2 foliation (*ca.* 2.2 wt% to *ca.* 1.4 wt%, respectively). Conversely, MnO and FeO result enriched within Cld$_2$ marking the foliation and depleted in Cld$_1$ included in Grt$_1$ (Table 3). Epidote crystals display a marked zonation with allanite cores and clinozoisite rims.

7. Carbonate carbon and oxygen isotope compositions

The main variations in C, O and Sr isotope compositions of carbonates from the CCU rock suite are shown in Figs. 7–10; a selection of isotopic data is provided in Table 3 and all the full isotopic dataset is reported in the supplementary Table 1 s. The $\delta^{18}O$ *vs.* $\delta^{13}C$ compositions of the various carbonate types described in the previous sections are reported in Fig. 7. All CSU calc-schists analyzed have $\delta^{18}O$ considerably lower than that of their likely marine carbonate protoliths (+28 to +30‰): this has been observed throughout the western Alps and has largely been interpreted as reflecting O isotope exchange at varying scales with metamorphosed terrigenous rocks, *via* fluids generated by dehydration reactions (see Cook-Collars et al., 2014, and the discussion by Epstein et al., 2020). However, most of the other lithologies at the Champorcher exposure (*e.g.*, the CCU) have even lower $\delta^{18}O$, as low as +13‰. In contrast, the $\delta^{13}C$ values of the CCU largely overlap with those of the sedimentary and ophiolitic protoliths (about −1.0 to +2.5‰). Carbonates from the CSU have higher $\delta^{18}O$ (+21.9 to +23.6‰) and lower $\delta^{13}C$ (+0.1 to −1.0‰) than carbonates from the basal ophicarbonates, the latter having $\delta^{18}O$ of +13.3 to +15.6‰ and $\delta^{13}C$ ranging from +1.8 to −0.5‰. Two ophicarbonate blocks within the calcschist unit show higher $\delta^{18}O$ values (+14.2 and + 17.5‰). Carbonates forming the matrix of the CCU and of the interlayered sedimentary mélange (SedMé in Fig. 7) are quite similar in isotope composition to carbonates from ophicarbonates, with $\delta^{18}O$ of +13.1 to +17.4‰ and $\delta^{13}C$ of −1.1 to +2.8‰. The sedimentary mélange samples display a narrower compositional range than the rest of the CCU (Fig. 7B). The isotopic compositions of the metasomatic horizon and of high-*P* veins mostly overlap the values of the CCU *s.s.* ($\delta^{18}O$ of +13.0 to +17.5‰; $\delta^{13}C$ of −0.1 to +1.7‰; Fig. 7C).

Analyses of serpentinite clasts and surrounding CCU matrix show decreased $\delta^{18}O$ values in the matrix, from +15.5 in clasts to +14.7‰ in the matrix (Fig. 8). $\delta^{18}O$ values as low as +13.6‰ were obtained for carbonates from high-*P* metamorphic veins. For all analyses plotted in Fig. 8, $\delta^{13}C$ is rather constant, ranging from +1.5 to +2.0‰.

The O, C and Sr isotope compositions of representative samples of the different CCU layers, of high-*P* metamorphic veins and of metasomatic horizons are shown in Fig. 9. The data show that the CCU sedimentary carbonates have Sr isotope compositions between Jurassic and Cretaceous seawater signatures (0.7070 and 0.7074, respectively; McArthur et al., 2001), while the high-*P* metamorphic veins and the metasomatic horizons are enriched in radiogenic Sr, showing $^{87}Sr/^{86}Sr$ ratios between 0.7077 and 0.7083.

8. Discussion

8.1. The Champorcher rock suite from oceanic to peak subduction conditions

The rock suite from the high Champorcher Valley corresponds to a seafloor sequence consisting of serpentinized lithospheric mantle overlain by carbonaceous clastic pelagic sediments. As proposed by Tartarotti et al. (2017, 2019) the sequence was deposited in an oceanic extensional setting, where mantle rocks exhumed at the seafloor by intra-oceanic detachment faults became prone to sedimentation of pelagic carbonates. Concomitant brecciation/erosion of the ultramafic bedrock released the ultramafic clasts that typify the CCU broken formation (Tartarotti et al., 2017).

During Alpine subduction, this oceanic rock package atop the downgoing oceanic plate, detached from the slab and was incorporated into the plate interface (Agard et al., 2018; Angiboust and Agard, 2010; Angiboust et al., 2009; Tartarotti et al., 2019). This explains the development of the D1-D2 shear deformation events associated with metamorphic recrystallization and *syn*-tectonic development of subduction-zone mineral assemblages that are well represented by the calcschists metasedimentary unit above the CCU and by the basal serpentinite.

In calcschists and micaschists, the prograde S_2 foliation provides a regional-scale marker to trace the *P-T* evolution of the full rock suite. The S_2 foliation in these rocks consist of Si-rich phengite + garnet + chloritoid + lawsonite (now pseudomorphosed) + zoisite. The *P-T* stability field of such an assemblage has been computed using the bulk composition of a representative micaschist sample CSA5 along with the

Table 3
C—O and $^{87}Sr/^{86}Sr$ isotopic composition of representative samples.

Lithologies	Sample	$\delta^{13}C$ (‰)	$\delta^{18}O$ (‰)	$^{87}Sr/^{86}Sr$	2σ	Carbonate
	DON 15–3	1.6	14.9	0.707385	0.000015	cal
	DON 15–4	1.4	13.5	0.707334	0.000019	cal
	MIS14	1.7	13.9	0.707050	0.000011	dol
Broken formation	MIS 3D	1.0	13.9	0.707202	0.000011	cal
	DON 15–9	1.0	16.3	0.708219	0.000008	dol
Metasomatic	DON 15–11	0.3	15.6	0.707991	0.000014	dol
high-*P* veins	DON 15–2	1.5	13.2	0.707649	0.000017	dol

$^{87}Sr/^{86}Sr$ data are not age corrected (low Rb/Sr ratio).
dol - dolomite; cal - calcite.
The complete C—O isotope data are reported in the Supplementary Table.

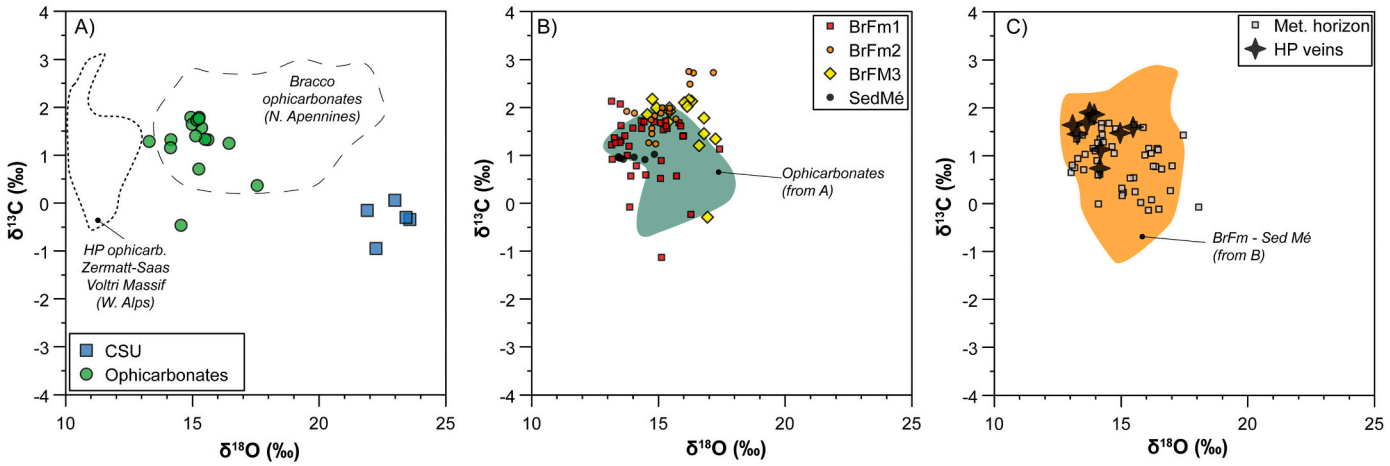

Fig. 7. $\delta^{13}C$ *vs.* $\delta^{18}O$ values of various carbonate from the CCU and CSU in the Champorcher ophiolite. (A) $\delta^{13}C$ *vs.* $\delta^{18}O$ values of carbonates from ophicarbonates and calcschists from the Champorcher ophiolite compared with ophicarbonates from the Zermatt-Saas and Voltri units (Western Alps) and from the Bracco unit (Northern Appennines). (B) $\delta^{13}C$ *vs.* $\delta^{18}O$ values of carbonates from the units composing the CCU compared with the field obtained from ophicarbonates (green dots in A). (C) $\delta^{13}C$ *vs.* $\delta^{18}O$ values of carbonates from metasomatic horizons and high-*P* veins from the CCU compared with the field obtained from broken formations and sedimentary mélange as showed in B. (For interpretation of the references to colour in this figure legend, the reader is referred to the web version of this article.)

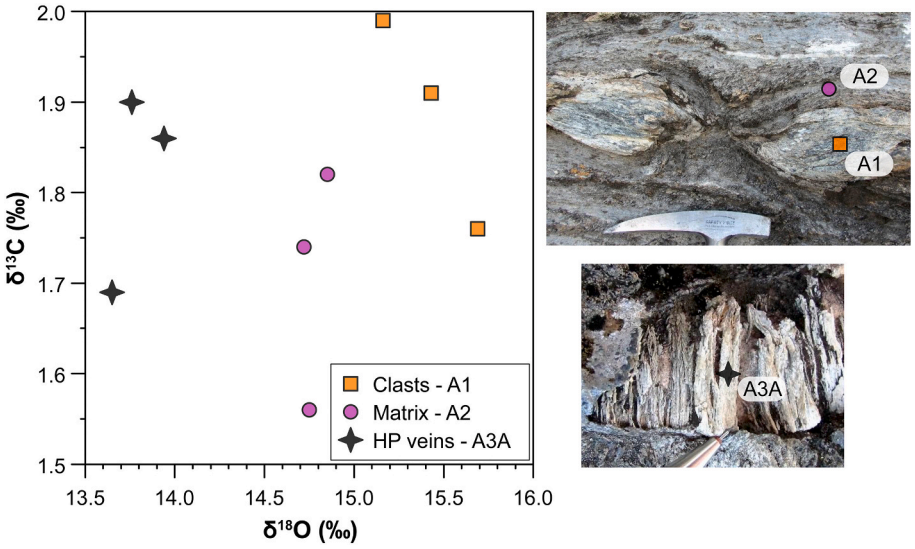

Fig. 8. (A) $\delta^{13}C$ *vs.* $\delta^{18}O$ values of carbonate from a profile through ultramafic clast – matrix and high-*P* vein within the CCU. (B) Field image referring to the exact position of the rock sampled for the isotope analysis. In particular, A1 is representative of ultramafic clast and A2 of the matrix. (C) Field image of the vein, filling a boudin neck (see also Fig. 2D and E) sampled for the isotopic analysis.

compositions of the syn-tectonic (S_2) rock forming minerals. Fig. 10 shows the *P-T* pseudosection computed using the system Si-Al-Fe-Mg-Ca-Na-K-Mn at water saturated conditions (for more details, see section *3.2 Thermodynamic modeling*). The diagram shows that average *P-T* conditions of 2.3 ± 0.1 Gpa and 500 ± 20 °C were achieved for the equilibrium crystallization of garnet + phengite + chloritoid + lawsonite, taking into account the isopleths of the Si content of syn-tectonic phengite and of the garnet composition. These peak *P-T* estimates for Champorcher agree with those provided for eclogites of the Zermatt-Saas Zone (2.2–2.4 GPa, 520–550 °C; Angiboust et al., 2009; Angiboust and Agard, 2010; Dragovic et al., 2020), but the T estimates are lower than those of Rebay et al. (2012; 2.0-2.5 GPa, 600 °C) and Luoni et al. (2018; 2.8-3.5 GPa, 600-670 °C) based on the study of the serpentinite.

A major difference between the Champorcher serpentinite presented here and the rest of the Mt. Avic massif and the whole Zermatt-Saas Zone is the lack of metamorphic olivine, Ti-clinohumite and Ti-chondrodite in the CCU. These phases are abundant in the classic Zermatt-Saas serpentinite (Li et al., 2004; Luoni et al., 2018; Gilio et al., 2019; Kempf et al., 2020; Rebay et al., 2012). The difference can be attributed either to the lower peak P-T conditions attained by the Champorcher rock-suite, or, more likely, to retrograde breakdown of olivine to antigorite during exhumation (see Dragovic et al., 2020).

8.2. *Metasomatic horizons: The rock markers of coupled decarbonation and carbonation processes*

Metasomatic horizons are widespread in the Champorcher rock suite, as presented here, and form along the contacts between carbonaceous (CCU and metasedimentary unit) and siliceous ultramafic rocks from various settings. As outlined by Rotondo et al. (2021), a major metasomatic horizon runs along the contact of CCU with the basal serpentinite: the horizon is rather continuous, made of dolomite + amphibole ± chlorite ± calcite ± oxides, and has been associated with

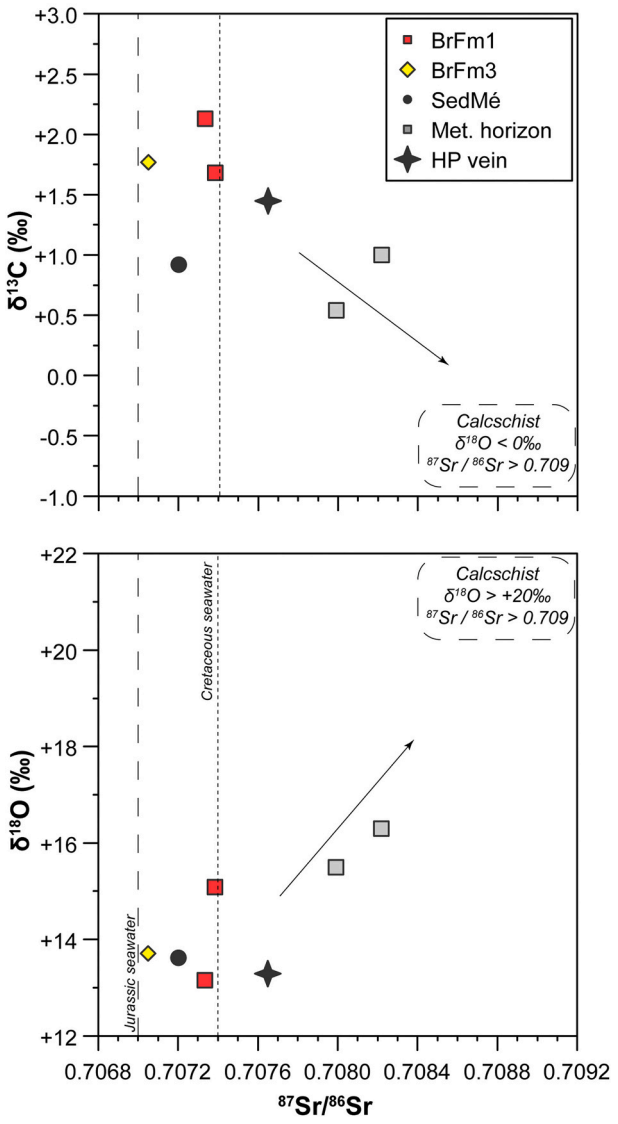

Fig. 9. (A) $\delta^{13}C$ values *vs.* $^{87}Sr/^{86}Sr$ of carbonate from representative samples of the different CCU layers. (B) $\delta^{13}O$ values *vs.* $^{87}Sr/^{86}Sr$.

influx of fluids sourced externally in the metasedimentary unit (Rotondo et al., 2021). Here, we point out that the metasomatic rocks do not only occur along the major serpentinite-CCU contact, but also form rinds in between the CCU ultramafic blocks and the associated matrix and/or the calcschists. A closer look at rock samples collected along profiles across the contacts, between ultramafic blocks and CCU matrix helps defining some key features of the fluid-driven element exchange between the two systems.

In detail, the CCU matrix near the contacts shows pervasive sets of pressure solution seams parallel to the S_2 peak foliation (Figs. 4D-E). These structures point to a fluid-mediated process that consumed rock-forming calcite to produce tremolite and diopside, with consequent release of carbonate-hosted CO_2 to the reacting fluid. Tremolite and diopside formation after calcite becomes dominant at the contact between CCU matrix and ultramafic blocks, where fluids become channeled (Fig. 4D, E). In such settings the calcite matrix represents a relict rock domain overgrown by Ca-bearing silicates (Figs. 4F, G, 5A, B). Remarkably, no graphite has been observed during Raman investigation, perhaps suggesting oxidized conditions associated with the pressure-dissolution process in a rock-buffered system.

In the associated serpentinite blocks, the rock domains in contact with the above-described CCU rocks and with the metasomatic rinds show an antigorite matrix replaced by a dense network of calcite veins (Figs. 2A, B, 5C). The replacement textures described above require fluid flow along the CCU dissolution planes and the matrix-block contacts and the release of CO_2 from calcite to a COH fluid. Reaction of this fluid with ultramafic rocks led to diffuse serpentinite carbonation (Figs. 4A-C), particularly near the contacts with the CCU limestones. The evidence that (i) in the CCU tremolite and diopside formed along pressure-solution planes parallel to the S_2 foliation (Figs. 4D-G) and that (ii) antigorite is the serpentine mineral overgrown by calcite, suggests that both decarbonation in the CCU and carbonation of nearby serpentinites took place during prograde subduction. Aragonite, rather than calcite, would certainly have been stable during the peak metamorphism of the CCU and aragonite was recently reported in high-*P* metamorphic marbles in the Combin Zone (Western Alps; Manzotti et al., 2021; *e.g.*, see the thermodynamic calculations by Cook-Collars et al., 2014). Aragonite back-reaction to calcite would have been afforded by the rapid kinetics of the aragonite to calcite transformation.

Meter-scale veins hosting dolomite + diopside + chlorite (Fig. 2F) occurring inside the larger blocks and the smaller veins with the same mineralogical composition in the necks of boudinaged ultramafic clasts (Figs. 2E, 4F, G), are other products of the circulating, prograde COH metamorphic fluid. Plausible *T* conditions can be fixed between 300 °C, the chrysotile to antigorite transition, and 450–500 °C, the olivine-in reaction in serpentinite systems (Schwartz et al., 2013). A similar process has been envisaged for other subduction occurrences of associated marble and serpentinite (Scambelluri et al., 2016).

Loss of C from the CCU matrix, at least at cm- to m-scales, could have occurred *via* carbonate dissolution in fluids during pressure solution or as the result of decarbonation reactions. If the metamorphic COH fluid attending these processes then interacted with reactive ultramafic rocks, carbonate crystallization could have resulted (as observed to some degree), limiting the scale of transport of the C released from the nearby matrix. Alternatively, COH fluid migration along pressure solution planes away from reactive rock types and without “downstream” precipitation of C-bearing phases could favor transport of carbonic fluids over larger length-scales within (*e.g.*, up-dip) or out of the plate interface. A comparable mechanism has been proposed for garnetite layers in calcschists and micaschists in the ultrahigh-*P* Lago di Cignana metaophiolite (W. Alps, Italy), which have been shown to form by rock compaction and garnet dissolution along stylolite planes (Van Schrojenstein Lantman et al., 2021). Pressure-dissolution of rocks during subduction-zone metamorphism should be considered when thinking of fluid drainage out of slabs, bringing to the genesis of complex COH fluids released when carbonate rocks occur at top-slab and/or plate interface settings (see the discussion by Epstein et al., 2020).

8.3. *Isotopic tracing of carbon cycling*

The microstructural evidence for C loss from the CCU matrix into subduction fluids, and its capture by the associated ultramafic blocks, can be further traced by the C—O and Sr isotope analysis of various generations of rock-forming carbonate from different textural settings within the Champorcher rock-suite (*e.g.,* Cannaò et al., 2020). Fig. 7A shows that carbonates from the two major end-members in the rock suite, the basal serpentinite-ophicarbonate and the calcschists of the metasedimentary unit atop the sequence, display different $\delta^{18}O$ and $\delta^{13}C$ variability from negative (−1‰), near 0‰ (for the calcschist), to positive values of +2‰ in terms of $\delta^{13}C$ (basal serpentinite-ophicarbonate). Figs. 7B, C and 11 point out the similarity in the $\delta^{18}O$ and $\delta^{13}C$ of the CCU carbonates with those from ophicarbonates, metasomatic rinds and veins cutting the ultramafic clasts. The dataset presented by Rotondo et al. (2021) showed differing, non-overlapping ranges in $\delta^{18}O$ of carbonates for the CCU and the MH, with ophicarbonates having even lower values than both the CCU and MH and calcschists having even higher values (ranging to nearly +25‰). The larger dataset presented here shows similarity in carbonate $\delta^{18}O$ for all rock types but the higher-

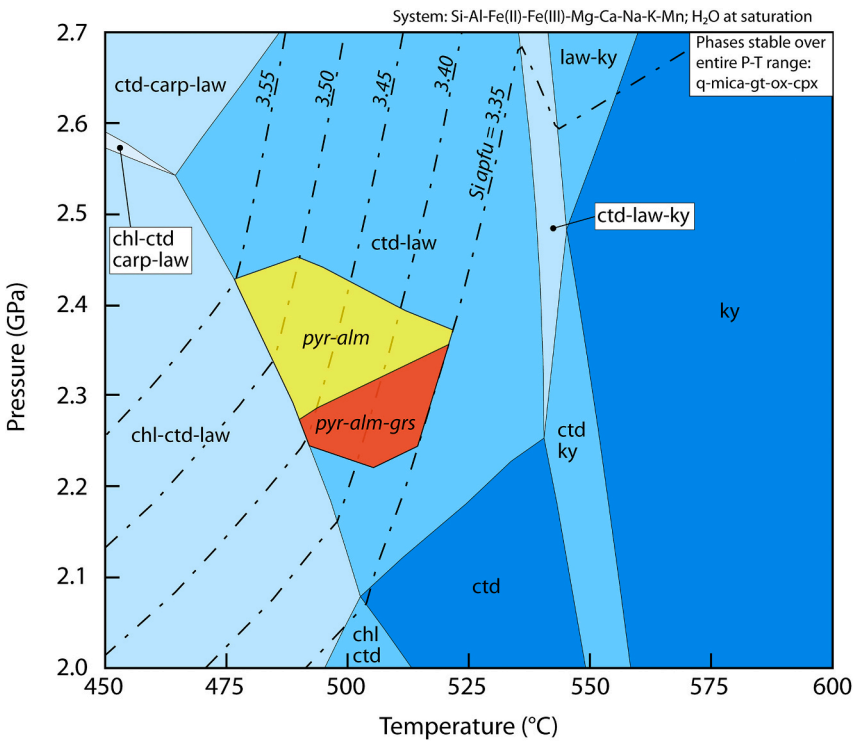

Fig. 10. Pseudosection for garnet-chloritoid sample CSA5 indicating peak P-T conditions of 2.3 ± 0.1GPa and 500 ± 20 °C. Dashed lines indicate Si-content of white mica in atoms per formula unit. The red and yellow fields indicate P-T estimates based on Si-content and garnet compositions from microprobe analysis, with the labels corresponding to the garnet isopleths which overlap in each region. Note that phases stable over the entire region are not indicated in a given field. The bulk rock composition is based on microprobe mineral analysis and point counting, and an assumed Fe^{3+}/Fe^{2+} = 0.2. Mineral abbreviations: carp: carpholite; chl: chlorite; cpx: clinopyroxene; ctd: chloritoid; gt: garnet; ilm:ilmenite; ky: kyanite; law: lawsonite; ox: Fe-oxide; q: quartz. Garnet endmember abbreviations are alm: almandine; grs: grossular; pyr: pyrope. Bulk composition in wt% oxide: SiO_2(57.0); Al_2O_3(17.9); FeO(9.63); Fe_2O_3(2.14); MgO (1.98); CaO(1.81); K_2O(2.53); Na_2O(0.56); MnO(1.09). (For interpretation of the references to colour in this figure legend, the reader is referred to the web version of this article.)

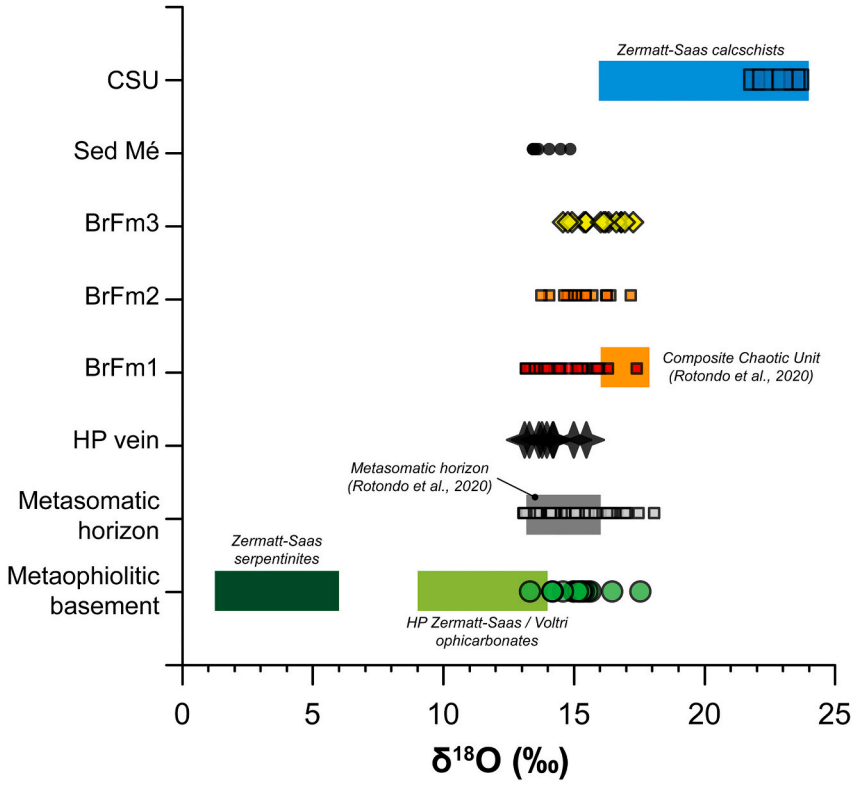

Fig. 11. $\delta^{18}O$ values of carbonate in each different unit composing the CCU. On the *y* axis the sequence of the units, from bottom to top, refers to the inferred lithostratigraphy. Results are compared with reference values. In detail, from bottom: range for serpentinites from the Zermatt-Saas Zone are from Cartwright and Barnicoat (1999) and refer to whole rock stable isotope analyses on serpentinites from Valtournanche and Mellichen ophiolites. Values for ophicarbonates from Zermatt-Saas and Voltri ophiolite units are from. Range for the metasomatic horizon and for BrFm1 are from samples from the same study area, analyzed by Rotondo et al. (2021). Values for calcschist from the Western Alps are from Cook-Kollars et al. (2014).

$\delta^{18}O$ calcschists (see Fig. 11). The data presented in this paper are suggestive of the interaction of all rock types in the Champorche suite, other than the calcschists, with a similar H_2O-rich fluid with $\delta^{18}O$ values indicative of some interaction or sourcing in mafic/ultramafic rocks, seemingly with some interaction with the metasedimentary rocks nearby (Figs. 7B, C, 9 and 10).

However, tackling this issue in more detail, the isotopic analysis of carbonates from (i) profiles through the boudinaged ultramafic blocks to the CCU matrix and (ii) extensional dolomite + diopside + chlorite veins in the boudins' necks shows common $\delta^{13}C$ compositions from +1.7 to +2.0‰, but $\delta^{18}O$ varying from values of +14.7 to +15.5‰ in the CCU matrix and in the clasts to $\delta^{18}O$ values about 1 to 2‰ lower in the

metamorphic veins (Fig. 8). Overall, this suggests the COH metamorphic vein fluid either records (1) involvement of an external fluid component, perhaps with a subset of the veins best representing the $\delta^{18}O$ of the fluids that infiltrated and lowered the $\delta^{18}O$ of the full CCU suite (to values of +13 to +18‰, considerably lower than the range exhibited regionally for the calcschists; see Epstein et al., 2020, 2021a), or (2) O isotope fractionation associated with dehydration reaction. Hypothesis (1), involving an external subduction fluid component in the fluid-mediated C cycling, is supported by the Sr isotope compositions of veins and metasomatic haloes. As portrayed for a relatively small number of samples in Fig. 9, while the Sr isotope composition of carbonates from the CCU matrix and clasts retain a Jurassic to Cretaceous seawater imprint (McArthur et al., 2001), the metamorphic veins and the metasomatic rinds are significantly enriched in radiogenic Sr. Compatible with the $\delta^{18}O$ values (Fig. 9B), the Sr isotope systematics also call for an involvement of externally-derived fluids bringing in radiogenic Sr likely leached from crustal slab reservoirs resembling the calcschist unit (*e.g.,* Cannaò et al., 2016, Cannaò et al., 2020). In particular, Fig. 9 displays the decoupling between the C—O isotopic composition of carbonates and their Sr isotopic ratios for the metasomatic horizon and the high-*P* veins formed within the boudins' necks. The slightly negative and positive correlations between $\delta^{13}C$ and $\delta^{18}O$ *vs.* $^{87}Sr/^{86}Sr$, respectively, support the partial re-equilibration of carbonates from the metasomatic horizon with fluids from a calcschist signature, in agreement with the observation provided by Rotondo et al. (2020). On the contrary, the rather constant $\delta^{13}C$ value of the high-*P* vein, similar with that of the CCU matrix, but slightly lower $\delta^{18}O$ (Figs. 7C, 8 and 9A) requires the influx of a ^{18}O-depleted fluids that likely match with a fluid sourced from a mafic-ultramafic reservoirs rather than from a sedimentary one (*e.g.,* Cannaò et al., 2020; Collins et al., 2015; Epstein et al., 2021a). Altogether, the O-C-Sr isotope systematics point to an interaction of the plate interface suite with a fluid bearing both mafic/ultramafic and sedimentary signatures. The calcschist unit containing some terrigenous component provided the radiogenic Sr signature (*i.e.*, reflecting decay of ^{87}Rb to elevate $^{87}Sr/^{86}Sr$) and an organic $\delta^{13}C$ signature. The low $\delta^{18}O$ imprint on the full CCU sequence was provided by the infiltrating H_2O-rich fluids. Whether or not the rocks in the CCU plate interface section were shifted in $^{87}Sr/^{86}Sr$ or $\delta^{13}C$, from their Jurassic seawater-inherited values (see Fig. 9), depended on the fluid:rock mass-balance of Sr and C during interaction. Some decrease in carbonate $\delta^{13}C$ could reflect effects of decarbonation within the sequence, with relatively heavy C fractionating into fluids released by these reactions (see Epstein et al., 2021a).

Our petrographic observations and thermodynamic modeling suggest that the Champorcher metasedimentary rocks underwent partial dehydration during their prograde path during the breakdown of chlorite. Chloritoid, present as inclusions in garnet and as syntectonic crystal along the high-*P* S_2 foliation (Fig. 6C) was probably stable until peak conditions. Chlorite dehydration was followed by lawsonite breakdown at higher *T,* possibly during peak to retrograde metamorphism (Fig. 10; see also Angiboust and Agard, 2010), as envisaged by the occurrence of lozenge-shaped pseudomorphs of paragonite + epidote + chlorite replacing lawsonite displaced along the S_1/S fabrics. Such a dehydration sequence is common for metasedimentary rocks exposed in the Western Alps (*e.g.,* Angiboust and Agard, 2010; Bebout et al., 2013; Manzotti et al., 2021) and other high-*P* metamorphic terranes worldwide. The fluid released by these reactions during the prograde burial of the metasedimentary rock, lying atop the CCU, transport the radiogenic Sr signatures strongly recorded in the metasomatic rocks. Despite the destabilization of lawsonite at *T* above the incipient dehydration of antigorite to form metamorphic olivine, which is lacking in the Champorcher ultramafic rocks, the high-*P* veins formed within the CCU are made of diopside + dolomite + chlorite that are stable at *T* compatible with that of lawsonite dehydration (Kerrick and Connolly, 1998). This evidence supports a coeval evolution for the devolatilization in the metasediments and the percolation of the fluids in part bearing a sedimentary signature, within the CCU, along an evolving, strongly deformed plate interface section reflecting focusing of both deformation and fluid infiltration (and associated metasomatism). Our observations support the suggestion by others that complexly deformed, transient plate interfaces act as major channels for fluid infiltration and mass transfer (*e.g.*, Jaeckel et al., 2018; Epstein et al., 2021a).

9. Conclusions

Here we provide an example of a deeply metamorphosed sedimentary/ophiolitic fragment that experienced *syn*-deformational fluid infiltration, likely involving fluids that affected the plate interface over a regional scale. The $\delta^{18}O$ range of carbonates in the metasedimentary cover (CSU) at this exposure appears to show the lowering observed over a regional scale and attributed to interaction with aqueous fluids derived from metamorphosing/devolatilizating terrigenous rocks (shales, sandstones; see Cook-Kollars et al., 2014; Epstein et al., 2020). This regional-scale infiltration tended to lower values to near $+22 \pm 2$‰ and many of the Champorcher rocks other than the CSU have lower values.

The work by Jaeckel et al. (2018) and Epstein et al. (2021a) demonstrated that, in some areas of particularly strong deformation, farther-traveled, lower-$\delta^{18}O$ fluids produced carbonate $\delta^{18}O$ comparable to the lower values at Champorcher. The $\delta^{18}O$ values calculated for these fluids are consistent with a more mafic/ultramafic source, perhaps within the subducting oceanic crustal section. It is possible that the CCU horizon exposed at Champorcher represents one of these zones of greater fluid flux affording infiltration by farther-traveled fluids.

The various metasomatic features at this locality indicated coeval, coupled decarbonation and carbonation resulting in fluid-mediated C redistribution along the deep subduction interface (at about 60 km depth) but conceivably without net loss and large-scale transport at the scale of the Champorcher exposures. Several other studies have demonstrated either net loss or net gain of C as carbonate and a major challenge of these field-based studies remains the connection of these scatter observations with meaningful consideration of larger (km to 10s of km)-scale C loss of a magnitude capable of impacting C cycling at an individual subduction margin. In this respect, the observation of tremolite and diopside-bearing pressure solution seams cutting through the Champorcher carbonatic CCU rocks point to C removal by fluid-mediated pressure dissolution which may bring to C loss out of the studied rock suite. Pressure dissolution processes have been shown to occur in other HP-UHP rocks (Van Schrojenstein Lantman et al., 2021) and pressure solution structures need to be further explored as potential channels of fluid loss from subducting slabs.

Declaration of Competing Interest

The authors declare that they have no known competing financial interests or personal relationships that could have appeared to influence the work reported in this paper.

Acknowledgements

We thank Samuel Angiboust and an anonymous referee for detailed and constructive reviews, and Nadia Malaspina for editorial handling. MS acknowledges the University of Genova for financial support and the Italian Ministry of Research for funding the PRIN 2017ZE49E7 project "The Dynamic Mass transfer from Slabs to Arcs". EC acknowledges funding by the Italian Society of Mineralogy and Petrology (SIMP award "Borsa di Studio per l'estero 2015") for supporting his visit to Lehigh University. Samuele Agostini is gratefully thanked for the generous access to the IGG-CNR laboratory. Fieldwork for GEB and GE, and the carbon and oxygen isotope analyses, were supported using funds from the Lehigh University College of Arts and Sciences and the Department of Earth and Environmental Sciences.

Appendix A. Supplementary data

Supplementary data to this article can be found online at https://doi.org/10.1016/j.lithos.2022.106813.

References

Agard, P., Plunder, A., Angiboust, S., Bonnet, G., Ruh, J., 2018. The subduction plate interface: rock record and mechanical coupling (from long to short timescales). Lithos 320-321, 537–566.

Ague, J.J., Nicolescu, S., 2014. Carbon dioxide released from subduction zones by fluid-mediated reactions. Nat. Geosci. 7, 355–360.

Angiboust, S., Agard, P., 2010. Initial water budget: the key to detaching large volumes of eclogitized oceanic crust along the subduction channel? Lithos 120 (3–4), 453–474.

Angiboust, S., Agard, P., Jolivet, L., Beyssac, O., 2009. The Zermatt-Saas ophiolite: the largest (60-km wide) and deepest (c. 70–80 km) continuous slice of oceanic lithosphere detached from a subduction zone? Terra Nova 21 (3), 171–180.

Bebout, G.E., 2014. Chemical and isotopic cycling in subduction zones. Treatise Geochem. 4 (20), 703–739.

Bebout, G.E., Agard, P., Kobayashi, K., Moriguti, T., Nakamura, E., 2013. Devolatilization history and trace element mobility in deeply subducted sedimentary rocks: Evidence from Western Alps HP/UHP suitesChemical. Geology 342, 1–20.

Bebout, G.E., Penniston-Dorland, S., 2016. Fluid and mass transfer at subduction interfaces—the field metamorphic record. Lithos 240-243, 228–258.

Beltrando, M., Rubatto, D., Compagnoni, R., Lister, G.S., 2007. Was the Valaisan basin floored by oceanic crust? Evidence of Permian magmatism in the Versoyen Unit (Valaisan Domain, Western Alps). Ofioliti 32, 85–99.

Beltrando, M., Lister, G., Hermann, J., Forster, M., Compagnoni, R., 2008. Deformation mode switches in the Penninic units of the Urtier Valley (Western Alps): evidence for a dynamic orogen. J. Struct. Geol. 30, 194–219.

Beltrando, M., Rubatto, D., Manatschal, G., 2010. Frompassive margins to orogens: The link between ocean-continent transition zones and (ultra)high-pressure metamorphism. Geology 38, 559–562.

Breeding, C.M., Ague, J.J., Bröcker, M., 2004. Fluid–metasedimentary interactions in sub- duction zone mélange: implications for the chemical composition of arc magmas. Geology 32, 1041–1044.

Bucher, K., Fazis, Y., DeCapitani, C., Grapes, R., 2005. Blueschists, eclogites, and decompression assemblages of the Zermatt-Saas ophiolite: high-pressure metamorphism of subducted Tethys lithosphere. Am. Mineral. 90, 821–835.

Caciagli, N.C., Manning, C.E., 2003. The solubility of calcite in water at 6_16 kbar and 500-800 °C. Contrib. Mineral. Petrol. 146, 275–285.

Cannaò, E., Malaspina, N., 2018. From oceanic to continental subduction: implications for the geochemical and redox evolution of the supra-subduction mantle. Geosphere 14, 2311–2336.

Cannaò, E., Scambelluri, M., Agostini, S., Tonarini, S., Godard, M., 2016. Linking serpentinite geochemistry with tectonic evolution at the subduction plate-interface: The Voltri Massif case study (Ligurian Western Alps, Italy). Geochim. Cosmochim. Acta 190, 115–133.

Cannaò, E., Scambelluri, M., Bebout, G.E., Agostini, S., Pettke, T., Godard, M., Crispini, L., 2020. Ophicarbonate evolution from seafloor to subduction and implications for deep-Earth C cycling. Chem. Geol. 546, 119626.

Collins, N.C., Bebout, G.E., Angiboust, S., Agard, P., Scambelluri, M., Crispini, L., John, T., 2015. Subduction-zone metamorphic pathway for deep carbon cycling: II. Evidence from HP/UHP metabasaltic rocks and ophicarbonates. Chem. Geol. 412, 132–150.

Connolly, J.A.D., 2005. Computation of phase equilibria by linear programming: a tool for geodynamic modeling and its application to subduction zone decarbonation. Earth Plan. Sci. Lett. 236, 524–541. https://doi.org/10.1016/j.epsl.2005.04.033.

Cook-Collars, J., Bebout, G.E., Collins, N.C., Angiboust, S., Agard, P., 2014. Subduction-zone metamorphic pathway for deep carbon cycling: I. Evidence from HP/UHP metasedimentary rocks, Italian Alps. Chem. Geol. 386, 31–48.

Cook-Kollars, J., Bebout, G.E., Collins, N.C., Angiboust, S., Agard, P., 2014. Subduction zone metamorphic pathway for deep carbon cycling: I. Evidence from HP/UHP metasedimentary rocks, Italian Alps. Chem. Geol. 386, 31–48. https://doi.org/10.1016/j.chemgeo.2014.07.013.

Dal Piaz, G.V., Cortiana, G., Del Moro, A., Martin, S., Pennacchioni, G., Tartarotti, P., 2001. Tertiary age and paleostructural inferences of the eclogitic imprint in the Austroalpine outliers and Zermatt-Saas ophiolite, Western Alps. Int. J. Earth Sciences (Geol Rundsch). 90, 668–684. https://doi.org/10.1007/s00530000177.

Dasgupta, R., 2013. Ingassing, storage, and outgassing of terrestrial carbon through geologic time. Rev. Mineral. Geochem. 75, 183–229.

Dasgupta, R., Hirschmann, M.M., 2010. The deep carbon cycle and melting in Earth's interior. Earth Planet. Sci. Lett. 298, 1–13.

Dolejs, D., Manning, C.E., 2010. Thermodynamic model for mineral solubility in aqueous fluids: Theory, calibration and application to model fluid-flow systems. Geofluids 10, 20–40.

Dragovic, B., Angiboust, S., Tappa, M.J., 2020. Petrochronological close-up on the thermal structure of a paleo-subduction zone (W. Alps). Earth Planet. Sci. Lett. 547, 116446.

Ellero, A., Loprieno, A., 2017. Nappe stack of Piemonte - Ligurian units south of Aosta Valley: New evidence from Urtier Valley (Western Alps). Geol. J. 1–20 https://doi.org/10.1002/gj.2984.

Epstein, G.S., Bebout, G.E., Angiboust, S., Agard, P., 2020. Scales of fluid-rock interaction and carbon mobility in the deeply underplated and HP-metamorphosed Schistes Lustrés, Western Alps. Lithos 354-355. https://doi.org/10.1016/j.lithos.2019.105229.

Epstein, G.S., Bebout, G.E., Angiboust, S., 2021a. Fluid and mass transfer along transient subduction interfaces in a deep paleo-accretionary wedge (W. Alps). Chem. Geol. 559 https://doi.org/10.1016/j.chemgeo.2020.119920.

Epstein, G.S., Bebout, G.E., Christenson, B.W., Sumino, H., Wada, I., Werner, C., Hilton, D.R., 2021b. Cycling of CO_2 and N_2 along the Hikurangi Subduction Margin, New Zealand: An integrated geological, theoretical, and isotopic approach. Geochemistry, Geophysics, and Geosystems. https://doi.org/10.1029/2021GC009650.

Festa, A., Pini, G.A., Dilek, Y., Codegone, G., 2010. Mélanges and mélange-forming processes: a historical overview and new concepts. Int. Geol. Rev. 52, 1040–1105.

Festa, A., Pini, G.A., Ogata, K., Dilek, Y., 2019. Diagnostic features and field-criteria in recognition of tectonic, sedimentary and diapiric mélanges in orogenic belts and exhumed subduction-accretion complexes. Gondwana Res. 74, 7–30. https://doi.org/10.1016/j.gr.2019.01.003.

Fontana, E., Tartarotti, P., Panseri, M., Buscemi, S., 2015. Geological map of the Mount Avic massif (Western Alps Ophiolites). Journal of Maps. 11 (1), 126–135. https://doi.org/10.1080/17445647.2014.959567.

Forshaw, J.B., Pattison, D.R.M., 2021. Ferrous/ferric (Fe^{2+}/Fe^{3+}) partitioning among silicates in metapelites. Contr. Miner. Petrol. 176 (9), 63. https://doi.org/10.1007/s00410-021-01814-4.

Frezzotti, M.L., Selverstone, J., Sharp, Z.D., Compagnoni, R., 2011. Carbonate dissolution during subduction revealed by diamond-bearing rocks from the Alps. Nat. Geosci. 4, 703–706.

Galvez, M., Beyssac, O., Martinez, I., Benzerara, K., Chaduteau, C., Malvoisin, B., Malavieille, J., 2013. Graphite formation by carbonate reduction during subduction. Nat. Geosci. 6, 473–477.

Gerya, T.V., Stöckhert, B., Perchuk, A.L., 2002. Exhumation of high-pressure metamorphic rocks in a subduction channel: a numerical simulation. Tectonics 21, 6–19.

Gilio, M., Scambelluri, M., Agostini, S., Godard, M., Peters, D., Pettke, T., 2019. Petrology and geochemistry of serpentinites associated with the ultra-high Pressure Lago di Cignana Unit (ItalianWestern Alps). J. Petrol. 60 (6), 1229–1262.

Giuntoli, F., Brovarone, A.V., Menegon, L., 2020. Feedback between high-pressure genesis of abiotic methane and strain localization in subducted carbonate rocks. Sci. Rep. 10 (1), 1–15.

Gorman, P.J., Kerrick, D.M., Connolly, J.A.D., 2006. Modeling open system metamorphic decarbonation of subducting slabs. Geochem. Geophys. Geosyst. 7, Q04007.

Green, E., Holland, T., Powell, R., 2007. An order-disorder model for omphacitic pyroxenes in the system jadeite-diopsidehedenbergite- acmite, with applications to eclogitic rocks. Am. Mineral. 92 (Issue 7), 1181–1189. https://doi.org/10.2138/am.2007.2401.

Groppo, C., Beltrando, M., Compagnoni, R., 2009. The P–T path of the ultra-high pressure Lago Di Cignana and adjoining high-pressure meta-ophiolitic units: insights into the evolution of the subducting Tethyan slab. J. Metamorph. Geol. 27, 207–231.

Haws, A.A., Starr, P.G., Dragovic, B., Scambelluri, M., Belmonte, D., Caddick, M.J., Broadwell, K.S., Ague, J.J., Baxter, E.F., 2020. Meta-rodingite dikes as recorders of subduction zone metamorphism and serpentinite dehydration: Voltri Ophiolite, Italy. Chem. Geol. 565, 120077.

Hawthorne, F.C., Oberti, R., Harlow, G.E., Maresch, W.V., Martin, R.F., Schumacher, J. C., Welch, M.D., 2012. Nomenclature of the amphibole supergroup. Am. Mineral. 97 (11−12), 2031–2048.

Hilton, D.R., Fischer, T.P., Marty, B., 2002. Noble gases and volatile recycling at subduction zones. In: Procelli, D., Ballentine, C.J., Wieler, R. (Eds.), Noble Gases in Cosmochemistry and Geochemistry (Pp. 319–370). Washington, D.C. Mineralogical Society of America. https://doi.org/10.1515/9781501509056-011 chap. 9.

Holland, T.J.B., Powell, R., 1991. A Compensated-Redlich-Kwong (CORK) equation for volumes and fugacities of CO_2 and H_2O in the range 1 bar to 50 kbar and 100–1600°C. Contr. Mineral. and Petrol. 109, 265–273. https://doi.org/10.1007/BF00306484.

Holland, T.J.B., Powell, R., 2011. An improved and extended internally consistent thermodynamic dataset for phases of petrological interest, involving a new equation of state for solids. J. Metamorph. Geol. 29, 333–383. https://doi.org/10.1111/j.1525-1314.2010.00923.x.

Jaeckel, K, Bebout, G.E., Angiboust, S., 2018. Deformation-enhanced fluid and mass transfer along Western and Central Alps paleo-subduction interfaces: Significance for carbon cycling models. Geosphere 14 (6), 2355–2375.

Jarrard, R.D., 2003. Subduction fluxes of water, carbon dioxide, chlorine, and potassium. Geochem. Geophys. Geosyst. 4, 8905. https://doi.org/10.1029/2002GC000392.

Kempf, E.D., Hermann, J., Reusser, E., Baumgartner, L.P., Lanari, P., 2020. The role of the antigorite + brucite to olivine reaction in subducted serpentinites (Zermatt, Switzerland). Swiss J. Geosci 113, 16.

Kerrick, D.M., Connolly, J.A.D., 1998. Subduction of ophicarbonates and recycling of CO_2 and H_2O. Geology 26 (4), 375–378.

Lagabrielle, Y., Cannat, M., 1990. Alpine Jurassic ophiolites resemble the modern Central Atlantic basement. Geology 18, 319–322.

Li, X.P., Rahn, M., Bucher, K., 2004. Serpentinites of the Zermatt-Saas ophiolite complex and their texture evolution. J. Metamorph. Geol. 22, 159–177.

Luoni, P., Rebay, G., Spalla, M.I., Zanoni, D., 2018. UHP Ti-chondrodite in the Zermatt-Saas serpentinite: Constraints on a new tectonic scenario. Am. Mineral. 103, 1002–1005.

Malaspina, N., Poli, S., Fumagalli, P., 2009. The oxidation state of metasomatized mantle wedge: insights from C–O–H-bearing garnet peridotite. J. Petrol. 50, 1533–1552.

Manzotti, P., Bosse, V., Pitra, P., Robyr, M., Schiavi, F., Ballevre, M., 2018. Exhumation rates in the Gran Paradiso Massif (Western Alps) constrained by in-situ Th-U-Pb dating of accessory phases (monazite, allanite and xenotime). Contributions to Mineralogy and Petrology 173. https://doi.org/10.1007/s00410-018-1452-7 art. N. 24.

Manzotti, P., Ballèvre, M., Pitra, P., Schiavi, F., 2021. Missing lawsonite and aragonite found: P–T and fluid composition in meta-marls from the Combin Zone (Western Alps). Contrib. Mineral. Petrol. 176, 60. https://doi.org/10.1007/s00410-021-01818-0.

Marroni, M., Pandolfi, L., 2007. The architecture of an incipient oceanic basin: a tentative reconstruction of the Jurassic Liguria-Piemonte basin along the Northern Apennines-Alpine Corsica transect. Int. J. Earth Sci. 96, 1059–1078.

Martin, S., Rebay, G., Kienast, J.R., Mevel, C., 2008. An eclogitized oceanic palaeo-hydrothermalfield from the St Marcelvalley (ItalianWestern Alps). Ofioliti 33, 49–63.

Massonne, H.J., Schreyer, W., 1989. Stability field of the high-pressure assemblage talc + phengite and two new phengite barometers. Eur. J. Mineral. 1 (3), 391–410.

McArthur, J.M., Howarth, R.J., Bailey, T.R., 2001. Strontium isotope stratigraphy: LOWESS version 3: best fit to the marine Sr-isotope curve for 0–509 Ma and accompanying look-up table for deriving numerical age. The Journal of Geology 109 (2), 155–170.

McCrea, J.M., 1950. On the isotopic chemistry of carbonates and a paleotemperature scale. J. Chem. Phys. 18, 849–857. https://doi.org/10.1063/1.1747785.

McInness, B.I.A., Cameron, E.H., 1994. Carbonated alkaline hybridizing melts from a subarc environment: mantle wedge samples from the Tabar-Lihir-Tanga-Feni arc, Papua-New Guinea. Earth Planet. Sci. Lett. 122, 125–141.

Menzel, M.D., Garrido, C.J., Sánchez-Vizcaíno, V.L., 2020. Fluid-mediated carbon release from serpentinite-hosted carbonates during dehydration of antigorite-serpentinite in subduction zones. Earth Planet. Sci. Lett. 531, 115964.

Molina, J.F., Poli, S., 2000. Carbonate stability and fluid composition in subducted oceanic crust: an experimental study on H_2O-CO_2-bearing basalts. Earth Planet. Sci. Lett. 176, 295–310.

Muñoz-Montecinos, J., Angiboust, S., Garcia, Casco A., Glodny, J., Bebout, G.E., 2021. Episodic hydrofracturing and large-scale flushing along deep subduction interfaces: Implications for fluid transfer and carbon recycling (Zagros Orogen, southeastern Iran). Chem. Geol. 571 (paper n.120173).

Paul, D., Skrzypek, G., 2007. Assessment of carbonate-phosphoric acid analytical technique performed using GasBench II in continuous flow isotope ratio mass spectrometry. Int. J. Mass Spectrom. https://doi.org/10.1016/j.ijms.2006.11.006.

Piccoli, F., Brovarone, A.V., Beyssac, O., Martinez, I., Ague, J.J., Chaduteau, C., 2016. Carbonation by fluid–rock interactions at high-pressure conditions: Implications for carbon cycling in subduction zones. Earth Planet. Sci. Lett. 445, 146–159. https://doi.org/10.1016/j.epsl.2016.03.045.

Poli, S., Franzolin, E., Fumagalli, P., Crottini, A., 2009. The transport of carbon and hydrogen in subducted oceanic crust: an experimental study to 5 GPa. Earth Planet. Sci. Lett. 278, 350–360.

Polino, R., Dal Piaz, G.V., Gosso, G., 1990. Tectonic erosion at the Adria margin and accretionary processes for the cretaceous orogeny of the Alps. Mémoire de la Société Géologique de France 156, 345–367.

Rebay, G., Spalla, M.I., Zanoni, D., 2012. Interaction of deformation and metamorphism during subductionand exhumation of hydrated oceanic mantle: Insights from theWestern Alps. J. Metamorphic Geol. 2012 (30), 687–702.

Rebay, G., Zanoni, D., Langone, A., Luoni, P., Tiepolo, M., Spalla, M.I., 2018. Dating of ultramafic rocks from the Western Alps ophiolites discloses late cretaceous subduction ages in the Zermatt-Saas Zone. Geol. Mag. 155 (2), 298–315. https://doi.org/10.1017/S0016756817000334.

Reinecke, T., 1991. Very high-pressure metamorphism and uplift of coesite-bearing metasediments from the Zermatt-Saas zone, Western Alps. Eur. J. Mineral. 3, 7–17.

Rotondo, F.C., Tartarotti, P., Guerini, S., Della Porta, G., Campomenosi, N., 2021. Metasomatic horizon sealing serpentinite-metasediments pair in the Zermatt-Saas metaophiolite (Northwestern Alps): record of a channel for focussed fluid flow during subduction. Ofioliti 46 (1), 1–25. https://doi.org/10.4454/ofioliti.v46i1.535.

Rotondo, F.C., Tartarotti, P., Guerini, S., Della Porta, G., Campomenosi, N., 2021. Metasomatic horizon sealing serpentinite-metasediments pair in the Zermatt-Saas metaophiolite (Northwestern Alps): record of a channel for focussed fluid flow during subduction. Ofioliti 46 (1), 1–25. https://doi.org/10.4454/ofioliti.v46i1.535.

Rubatto, D., Gebauer, D., Compagnoni, R., 1999. Dating of eclogite-facies zircons: the age of Alpine metamorphism in the Sesia-Lanzo Zone (Western Alps). Earth Planet. Sci. Lett. 167, 141–158.

Ruh, J.B., Le Pourhiet, L., Agard, P., Burov, E., Gerya, T., 2015. Tectonic slicing of subducting oceanic crust along plate interfaces: Numerical modeling. Geochem. Geophys. Geosyst. 16, 3505–3531.

Sanchez-Valle, C., Martinez, I., Daniel, I., Philippot, P., Bohic, S., Simionovici, A., 2003. Dissolution of strontianite at high P-T conditions: an in-situ synchrotron X-ray fluorescence study. Am. Mineral. 88, 978–985.

Sapienza, G.T., Scambelluri, M., Braga, R., 2009. Dolomite-bearing orogenic garnet peridotites witness fluid-mediated carbon recycling in a mantle wedge (Ulten Zone, Eastern Alps, Italy). Contrib. Mineral. Petrol. 158, 401–420.

Scambelluri, M., Bebout, G.E., Belmonte, D., Gilio, M., Campomenosi, N., Collins, N., Crispini, L., 2016. Carbonation of subduction-zone serpentinite (high-pressure ophicarbonate; Ligurian Western Alps) and implications for the deep carbon cycling. Earth Planet. Sci. Lett. 441, 155–166.

Schwartz, S., Guillot, S., Reynard, B., Lafay, R., Debret, B., Nicollet, C., Lanari, P., Auzende, A.L., 2013. Pressure–temperature estimates of the lizardite/antigorite transition in high pressure serpentinites. Lithos 178, 197–210.

Sharma, S. Das, Patil, D.J., Gopalan, K., 2002. Temperature dependence of oxygen isotope fractionation of CO_2 from magnesite-phosphoric acid reaction. Geochim. Cosmochim. Acta 66, 589–592. https://doi.org/10.1016/S0016-7037(01)00833-X.

Starr, P.G., Broadwell, K.S., Dragovic, B., Scambelluri, M., Haws, A.A., Caddick, M.J., Smye, A.J., Baxter, E.F., 2020. The subduction and exhumation history of the Voltri Ophiolite, Italy: Evaluating exhumation mechanisms for high-pressure metamorphic massifs. Lithos 376–377, 105767.

Stöckhert, B., 2002. Stress and deformation in subduction zones: insight from the record of exhumed metamorphic rocks. Geol. Soc. Lond., Spec. Publ. 200, 255–274. https://doi.org/10.1144/GSL.SP.2001.200.01.15.

Stöckhert, B., Duyster, J., Trepmann, C., Massonne, H.J., 2001. Microdiamond daughter crystals precipitated from supercritical COH plus silicate fluids included in garnet, Erzgebirge, Germany. Geology 29, 391–394.

Tartarotti, P., Festa, A., Benciolini, L., Balestro, G., 2017. Record of Jurassic mass transport processes through the orogenic cycle: Understanding chaotic rock units in the high-pressure Zermatt-Saas ophiolite (Western Alps). Lithosphere 9, 399–407.

Tartarotti, P., Guerini, S., Rotondo, F., Festa, A., Balestro, G., Bebout, G.E., Cannaò, E., Epstein, G.S., Scambelluri, M., 2019. Superposed Sedimentary and Tectonic Block-In-Matrix Fabrics in a Subducted Serpentinite Mélange (High-pressure Zermatt Saas Ophiolite, Western Alps). Geosciences 9, 358.

Thomsen, T.B., Schmidt, M.W., 2008. The biotite to phengite reaction and mica-dominated melting in fluid carbonate-saturated pelites at high pressures. J. Petrol. 49, 1889–1914.

Tumiati, S., Martin, S., Godard, G., 2010. Hydrothermal origin of manganese in the high-pressure ophiolite metasediments of Praborna ore deposit (Aosta Valley, Western Alps). Eur. J. Mineral. 22, 577–594.

Van Roermund, H.L.M., Carswell, D.A., Drury, M.R., Heijboer, T.C., 2002. Microdiamonds in a megacrystic garnet websterite pod from Bardane on the island of Fjortoft, western Norway: evidence for diamond formation in mantle rocks during deep continental subduction. Geology 30, 959–962.

Van Schrojenstein Lantman, H.W., Scambelluri, M., Gilio, M., Wallis, D., Alvaro, M., 2021. Extensive fluid–rock interaction and pressure solution in a UHP fluid pathway recorded by garnetite, Lago di Cignana, Western Alps. J Metamorph Geol. 39, 501–518.

Vitale Brovarone, A., Martinez, I., Elmaleh, A., et al., 2017. Massive production of abiotic methane during subduction evidenced in metamorphosed ophicarbonates from the Italian Alps. Nat. Commun. 8, 14134. https://doi.org/10.1038/ncomms14134.

White, R.W., Powell, R., Holland, T.J.B., Johnson, T.E., Green, E.C.R., 2014. New mineral activity–composition relations for thermodynamic calculations in metapelitic systems. J. Metamorph. Geol. 32, 261–286. https://doi.org/10.1111/jmg.12071.